

IMPERIAL COLLEGE LONDON

DEPARTMENT OF AERONAUTICS

Aircraft Vehicle Design Report

Authors: Group 21

Angeliki Tzola	(01414569)
Iaroslav Kazakov	(01334502)
Stavros Sikkis	(01340226)
Niccolo Albaek	(01349577)
Isaias Araya	(01354590)

Academic Supervisor: Errikos Levis

Date of Deadline: 22 November 2019

Contents

1 Initial Weight, Thrust And Wing Modifications	1
2 Fuselage Design And Sizing	1
2.1 Introduction	1
2.2 Cabin Design	1
2.2.1 Cabin Layout And Service Considerations	1
2.2.2 Emergency Exits, Doors And Windows	1
2.2.3 Aircraft's Underbelly And Luggage Storage	2
2.2.4 Overall Cabin Layout And Dimensions	2
2.3 Flight Desk Design	3
2.3.1 Recommended Flight Deck Dimensions And Requirements	3
2.3.2 Aerodynamic Considerations And Design Choices	3
2.4 Fuselage Tail Design	3
2.5 Fuselage Dimensions	3
3 Wing Design	3
3.1 Aerofoil Selection Requirements	3
3.1.1 NACA 6-Series	3
3.1.2 WASP Aerofoil	4
3.1.3 Supercritical Aerofoils	4
3.1.4 Final Selection; NASA 04 ₍₂₎ 14	4
3.1.5 Thickness To Chord Ratio t/c	6
3.2 Sweep Angle $\Lambda_{c/4}$	6
3.2.1 Effects Of Sweep	6
3.3 Taper Ratio λ	7
3.4 Twist ϵ_t	7
3.5 Aspect Ratio AR	7
3.6 Dihedral	7
4 Aerodynamics Analysis - Wing Lift	8
4.1 Zero-Lift Angle Of Attack	8
4.2 Maximum Lift Coefficient Of The Wing	8
4.3 Lift Curve Slope Of The Wing	8
4.3.1 Wing Setting Angle	8
5 High Lift Device Selection & Sizing	8
5.1 Leading Edge Flaps	9
5.2 Trailing Edge Flaps	9
6 Aircraft System Layout Design	9
6.1 Fuel System	9
6.2 Hydraulic System	10
6.3 Pneumatic System	10
6.4 Electrical System	11
6.4.1 More Electrical Aircraft (MEA)	11
6.4.2 Auxiliary Power Unit (APU)	12
6.5 Actuators	12
6.6 Avionics	12
7 Weight & Balance Predictions	12
8 Powerplant Selection, Installation & Integration	14
8.1 Uninstalled Thrust	14
8.2 Nacelle Design	15
8.3 Engine Location And Pylons	16

9 Undercarriage	16
9.1 Constraints And Strut Loads	16
9.2 Tire Selection	17
9.3 ACN Estimation	17
9.4 Oleo Sizing	18
9.5 Retraction Mechanism And Discussion	18
10 Structural Layout	19
10.1 Wings	19
10.2 Tailplane	20
10.3 Fuselage	20
10.4 Landing-Gear	20
10.5 Aero-elastic Effects	20
11 Tailplane Sizing And Design	20
11.1 Horizontal Tailplane	21
11.1.1 Disposition	21
11.1.2 Area	21
11.1.3 Aspect Ratio (AR)	22
11.1.4 Aerofoil Selection	22
11.1.5 Sweep	22
11.1.6 Taper Ratio	22
11.2 Vertical Tailplane	22
11.2.1 Disposition	22
11.2.2 Area	22
11.2.3 Aspect Ratio (AR)	23
11.2.4 Taper Ratio	23
11.2.5 Aerofoil Selection	23
11.2.6 Sweep	23
12 Aerodynamic Analysis - Tail Lift	24
12.1 Horizontal Tail	24
12.2 Vertical Tail	25
13 Control Surface Design	25
13.1 Ailerons	25
13.1.1 Aileron Location Along Wing Span	25
13.1.2 Chord-ratio (c_a/c_w) And Planform Area (S_a)	25
13.1.3 Maximum Deflections ($\delta_{a_{max}}$)	26
13.2 Elevator	26
13.2.1 Span-ratio	26
13.2.2 Chord-ratio (c_e/c_H) And Planform Area (S_e)	26
13.2.3 Maximum deflections ($\delta_{e_{max}}$)	26
13.3 Rudder	26
13.3.1 Span-ratio (b_r/b_v)	27
13.3.2 Chord-ratio(c_r/c_v) and Planform Area (S_r)	27
13.3.3 Maximum deflections ($\delta_{r_{max}}$)	27
14 Static Stability	27
14.1 Longitudinal Static Stability	27
14.1.1 Power-Off and Power-On	27
14.2 Lateral Static Stability	28
14.3 Directional Static Stability	28
15 Aerodynamic Analysis - Drag Estimation	28
15.1 Zero-Lift Drag, C_{D_0}	29
15.1.1 Skin Friction Drag, C_f	29
15.1.2 FF_i And Q_i	30
15.1.3 $C_{D_{misc}}$	31
15.1.4 Wave Drag And Sweep	31
15.1.5 Overall Drag, C_D	33

16 Trim Analysis	34
17 Performance Estimation	37
17.1 Takeoff Distance	37
17.2 Balanced Field Length	37
17.3 Landing	37
17.4 Range, Endurance and Specific excess power	37
18 Discussion Of Overall Design	38
References	40
19 Appendix	42
19.1 Appendix 1	42
19.1.1 Prandtl-Glauert correction	42
19.1.2 Aspect ratio variation	42
19.1.3 Sweep angle at the leading edge equation	42
19.1.4 Twist angle ϵ_t	42
19.1.5 Effect of flaps in the wing zero-Lift angle of attack	42
19.1.6 Parameters affecting the zero Lift angle of attack	43
19.1.7 Wing Lift curve slope equation	43
19.2 Appendix 2	43
19.3 Appendix 3	44
19.4 Appendix 4	44
19.5 Appendix 5	45
19.6 Appendix 6	45
19.7 Appendix 7	46
19.8 Appendix 8	47
19.9 Appendix 9	48
19.10 Appendix 10	49
19.11 Appendix 11	49

1 Initial Weight, Thrust And Wing Modifications

Due to the lack of analytical tools, Winglets and Kuchemann body at the tail plane were removed from the aircraft baseline configuration. The weight of baggage allowed per passenger reduced to 20kg from 30kg. $C_{L_{max}}$ increased from 2.5 to 3 to increase wing loading by easing the take-off constraint, this is done by increasing the $\Delta C_{L_{max}}$ from flaps deployment by replacing fowler type with triple slotted flaps. The cruise altitude after diversion was increased from 15,000 ft to 20,000 ft as recommended by a project officer. These changes led to the following results: $MTOW = 15592\text{kg}$, fuel weight=2216kg Empty weight=8050kg, $MLW = 13990\text{kg}$, Payload weight =4925kg, Crew weight and their personal belongings =400kg. Wing loading was calculated to be 4118N/m^2 and the thrust-to-weight ratio of = 0.36. The revised thrust-to-weight is included in Appendix 8.

2 Fuselage Design And Sizing

2.1 Introduction

When designing the fuselage for a transport aircraft, the optimal shape was given by using a cylindrical mid-section for the following reasons: simplified structural design and manufacture, efficient internal layout with little loss of space, improved flexibility of the seating arrangement and further development by increasing the length of the fuselage were facilitated. However, a fineness ratio of more than 12 had to be avoided because of stiffness problems. The overall fuselage length and cross-section highly depended on the comfort of the passenger, which relied on a series of factors such as design and arrangement of seats, number of lavatories, stewardess services, etc. Therefore, comfort was one of the primary concerns when designing the fuselage.

2.2 Cabin Design

2.2.1 Cabin Layout And Service Considerations

The first step when designing the cabin was to decide upon the number of seats abreast. According to [28], the recommended number of seats abreast for a 50-passenger aircraft is four. Having three seats abreast would have given a “too slender” configuration, while five seats abreast would mean large diameter, thus increased drag. Having chosen four seats abreast, the next step was to determine the aisle and seat dimensions, as well as the number of lavatories and the galley volume. Using the information given in [1] see Appendix 19.7, and taking into consideration the comfort of the passengers for the 2,000km flight, the following parameters were determined:

- Headroom at aisle: 1.95m
- Aisle width: 0.50m
- Headroom at seat: 1.65m
- Seat width: 0.50m
- Seat height: 1.00m
- Seat pitch: 0.80m
- Galley volume: 2.50m³
- Number of lavatories (1m x 1m): 2

This implied a minimum cabin width of 2.50m when considering seating arrangement. The reasoning behind this selection of parameters was to provide a decent level of comfort (i.e. not looking for the minimum values as possible) while remaining in the “economy class” dimensions as an all “first-class” layout is unlikely to exist for a regional passenger aircraft. As the duration of the flight is around three hours, the choice of two lavatories instead of one was considered more appropriate, and a galley volume of 2.50m³ sufficient.

2.2.2 Emergency Exits, Doors And Windows

According to [27] and [3], for a seating capacity of 50 passengers one type I and one type IV emergency exits are required on each side of the fuselage. Their dimensions and requirements are shown in the Appendix 19.7. However, because of the high wing configuration, type IV exits were replaced with exits with dimensions of type III exits. The recommended seat pitches next to the emergency exits are 36 inches for type I and 18 inches for type III, which will affect the total cabin length. As the number of passengers in the aircraft was less than 70, one passenger door was sufficient. As height was not a significant constraint in this design, a gate of dimensions 1.80x0.90m² can replace one of the two types I emergency exits. Finally according to [3], windows will have a 0.50m pitch and were placed such that the top is roughly at the passenger’s eye level.

2.2.3 Aircraft's Underbelly And Luggage Storage

Because of the high mounted wing configuration, it was not possible to have the main landing retracting off the wing, part of which would locate in the belly of the aircraft. To have enough space to accommodate the luggage and the undercarriage, the cargo compartment height was established at 90cm. This decision reduced the length of the aircraft and moved the CG location more foremost as opposed to the tail cargo compartment. Considering an average luggage weight of 16kg per passenger, the total luggage weight in the underbelly was of 800kg. As the mean baggage density is of 200Kg/m^3 , with a loading efficiency of 0.75 the required volume for the luggage was found to be 5.33m^3 which did not require a length of more than 3m in the underbelly.

2.2.4 Overall Cabin Layout And Dimensions

Through simple calculations, it was obvious the most constraining dimension was the z-direction as the aisle height, and the underbelly height combined turned out to be bigger than the minimum cabin width. Considering also a floor thickness of $0.05D_{FUS}$, an internal fuselage diameter of 3.20m was obtained as shown in Figure 1.

The external fuselage diameter was found from the internal fuselage dimensions by adding 10cm for the thickness of the cabin wall. This configuration allowed more flexibility for the seating arrangement and comfort for the passenger. As the cabin width is not the major constraint, the passenger cabin can be part of the fuselage nose and tail as reducing the diameter won't affect the comfort of the passenger until we reach an inner diameter of 2.5m . This proves to be an advantage as the tail starts to be at angle more forward and therefore the total fuselage length will be reduced.

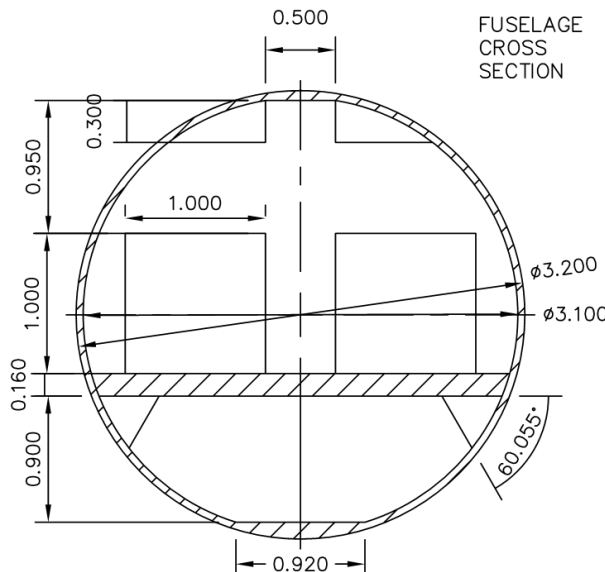


Figure 1: Fuselage cross-section

The cabin layout design is described in Figure 2. This arrangement was found to be the most volume efficient and gave a total length of 14m. The primary component which affected the length of the cabin was the number of rows. As the pitch was chosen to be 0.8m, having 13 rows on one side and 12 on the other occupied 10.4m and 9.6m respectively. Other components affecting the cabin length were the dimensions of the toilet and the galley. The first being 1m and latter 0.5m were obtained dividing the galley volume by the cabin cross-sectional area. Galleys also needed a 1m cross-aisle in front of them. This cross-aisle was also used to facilitate the path emergency exits at the cabin back.

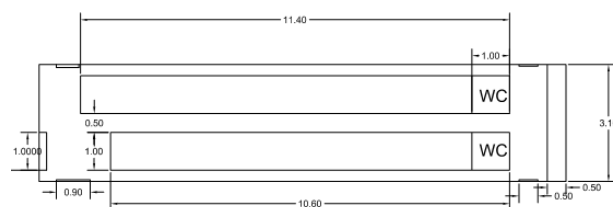


Figure 2: Cabin layout

2.3 Flight Deck Design

2.3.1 Recommended Flight Deck Dimensions And Requirements

When designing the flight deck of an aircraft, some of the key points to take into account were pilot positioning, visibility standards and aerodynamic considerations. Looking at similar aircraft and recommended dimensions for transport aircraft in [3], the following dimensions were estimated. A length of $3m$ was determined for the flight deck to accommodate pilots and contain flight instruments, avionics system and the controls systems. The minimum height requirement for the cabin at the pilot seat position was found to be $1.32m$, whereas the horizontal distance from the reference eye point to the windshield to be around $50/60cm$. Moreover, a minimum angle of (17°) from the horizontal line of sight was recommended for visibility considerations.

2.3.2 Aerodynamic Considerations And Design Choices

According to [29]: "Below Mach 0.8, the nose pressure drag is essentially zero for all shapes. The major significant factor is friction drag, which is largely dependent upon the wetted area, the surface smoothness of that area, and the presence of any discontinuities in shape. In the strictly subsonic model, a short, blunt, smooth elliptical shape is usually best". As the aircraft is travelling at Mach 0.75, a sharp nose cone design was not needed, and therefore a blunt nose shape was chosen. To minimise drag due to sudden change of sections, the windshield angle (35°) was chosen to be equal to the nose cone angle. This angle implied a nose cone of a length of approximately $0.5m$ in which the weather radar was installed. From looking at similar aircraft, the nose fineness ratio was around 1.7, which gave a total nose length of $5.5m$ for the diameter dimension.

2.4 Fuselage Tail Design

To design the fuselage tail, the fuselage tail angle of (17°) was found from looking at typical values for regional jet aircraft [30]. Then, a diameter of $0.6m$ at the end of the fuselage tail was chosen as a compromise between aerodynamic considerations and the APU exhaust system design. Using simple geometry, the fuselage tail length obtained was $8.5m$, of which the first $3.5m$ were occupied by the passenger cabin, and the rest by the APU and other systems.

2.5 Fuselage Dimensions

Using the lengths provided in the previous sections, the total length of the fuselage was estimated subtracting the lengths of the passenger cabin which are inside the nose ($2m$) and tail ($3.5m$) sections, to the sum of nose, passenger cabin and tail lengths previously calculated. This resulted in a total fuselage length of $22.5m$, and can be seen in 19.11.

3 Wing Design

3.1 Aerofoil Selection Requirements

To achieve operational suitability for high subsonic speeds during cruise at $M = 0.8$, categories of supercritical aerofoils and NACA 6-series were initially selected based on the highest C_L/C_D ratio at the cruise Reynolds number $Re = 18 \cdot 10^6$ at the desired cruise lift coefficient of $C_L = 0.4316$. Low profile drag coefficient during the cruise as well as in high lift conditions such as climb and cruise, maximum lift coefficient and gradual stalling characteristics especially at the tip were also considered by adding twist. To achieve a trimmed and stable cruise, small pitching moment coefficient and low skin friction coefficient were taken into account. Compressibility effects, such as critical Mach number or Drag divergence Mach number over the sectional surface due to high subsonic speeds were taken into account by adjusting the thickness to chord ratio and the sweep angle[3]. Additional characteristics such as a good pressure distribution for different angles of attack on the aerofoil surface as well as post-stall behaviour were examined. To ensure a safe take-off and landing, the greater the maximum α_{stall} , thus the danger of stall during take-off is minimised. However, it was sufficient to precisely select an angle of attack during take-off such that there was also no danger of a tail-strike.

3.1.1 NACA 6-Series

The NACA 6 series aerofoils can achieve a relatively high C_{Lmax} , but their main advantage is the ability to maintain low profile drag within the range of the C_L at cruise. In the laminar boundary layer regime, there is a stable pressure distribution without pressure peaks, keeping the local velocities low. However, the separation of the turbulent boundary layer in the rear part will limit the extent of the laminar layer. However, low super-velocities on these aerofoils also favour the attainment of a high critical Mach number which allows the usage of less swept wings[3]. For high

subsonic speeds, the effects of compressibility as described by the potential flow methods can result in a critical Mach number of the 0.73 for example in the case of the 64₂15 as shown in the image below. To account for that critical Mach number a sweep angle of 25° to 28° is needed to avoid strong shock formation inside the sonic region. The usage of thinner NACA aerofoils such as 64₂12 will result in a smaller sweep angle of approximately 22°.

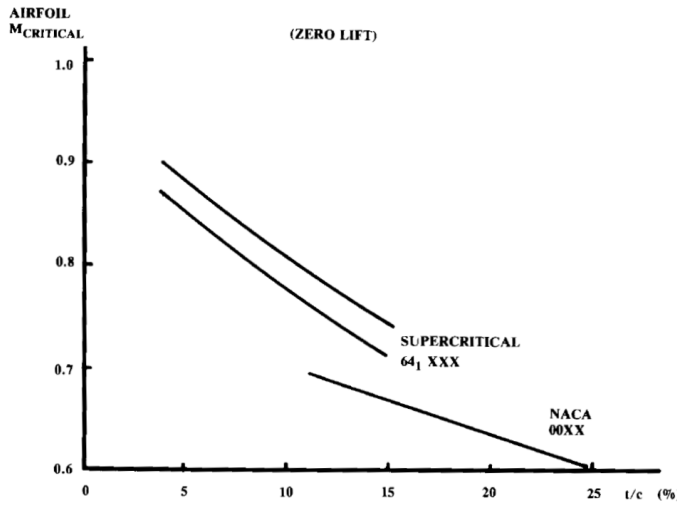


Figure 3: aerofoil critical Mach number relative to the thickness to chord ratio (t/c) [1]. It can be observed that the thinner aerofoil -i.e less t/c - the higher the M_{crit} and thus less sweep is needed.

3.1.2 WASP Aerofoil

Wasp aerofoil is an aerofoil with 9.4% t/c designed for thermal duration seaplanes. The purpose of its design indicates that it has been mainly tested and used for low boundary layer regimes (i.e data existing up to a Reynolds number of 300,000.) and mainly laminar boundary layer over the section so it can be possible to show unexpected strong compressibility effects such as shocks in higher Re within a turbulent boundary layer regime. The XFOIL data indicated a high C_l/C_d , however the experimental data found for lower Reynolds number did not match such a good performance, as that low thickness might have been sensitive to manufacturing variations by adding more weight which would not be encountered by the smaller sweep angle [8].

3.1.3 Supercritical Aerofoils

The purpose of this design approach is that in such shapes the upper aerofoil surface is flattened to reduce the flow acceleration and have increased camber aft sections where the majority of lift is generated. They have been initially designed to achieve higher critical Mach numbers by producing the same amount of lift, such that less sweep is needed [3]. At the critical Mach number inside the sonic regime, there is no fear of the formation of a strong shockwave and a much weaker one is usually formed, which allows considering crucial compressibility effects when the Drag Divergence Mach number is locally reached which is always greater than the critical Mach number and thus less sweep angle is needed [6].

3.1.4 Final Selection; NASA 04₍₂₎14

The key characteristics the final selection was based on were high c_l/c_d for the specific cruise angle of attack to maximise the lift generated, relatively low t/c, and sufficient cl for take off -and landing- without being close to stall regime.

When comparing the NACA 6 series aerofoil 64₂15 and the supercritical NASA 04₍₂₎14, except for the fact that NASA has the highest C_{LMAX} it is worth noting that for the case of the NACA aerofoils more sweep will be needed based on the critical Mach number which will further penalise the L/D ratio as in the sonic regime, strong shock-waves will form resulting in separated boundary layers at the trailing edge. Inside the sonic region of a supercritical aerofoil, series of oblique compression shockwaves are being formed resulting in weak shock-wave formation at the trailing edge [6]. As figures (1) and (2a) indicate, the critical Mach number in the case of the supercritical aerofoils is higher, reducing the required sweep. According to Figure (2b), the Drag coefficient variation as the Mach number increases remains lower for supercritical aerofoils. XFOIL data have also shown lower pitching moment coefficient for the supercritical aerofoils which is advantageous for stability reasons especially in post stall behaviour. Note that it is assumed that the

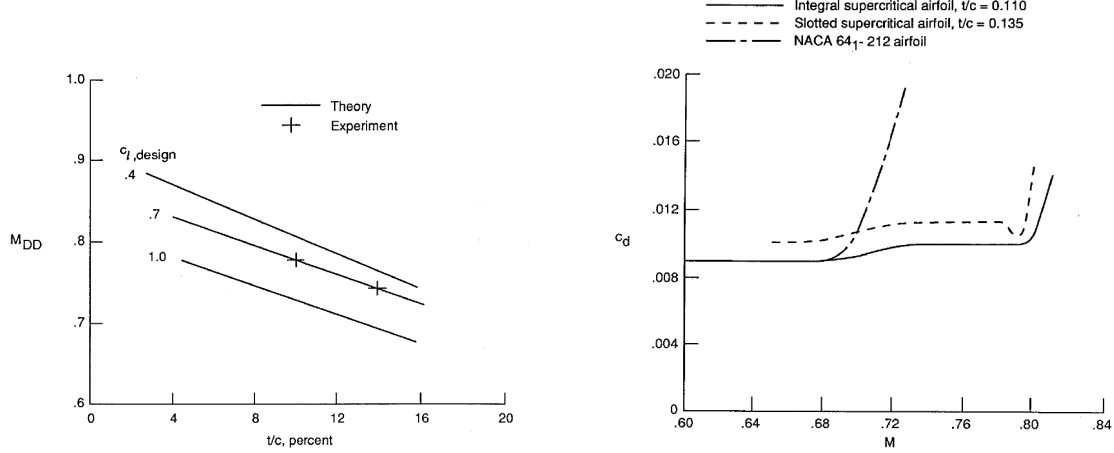
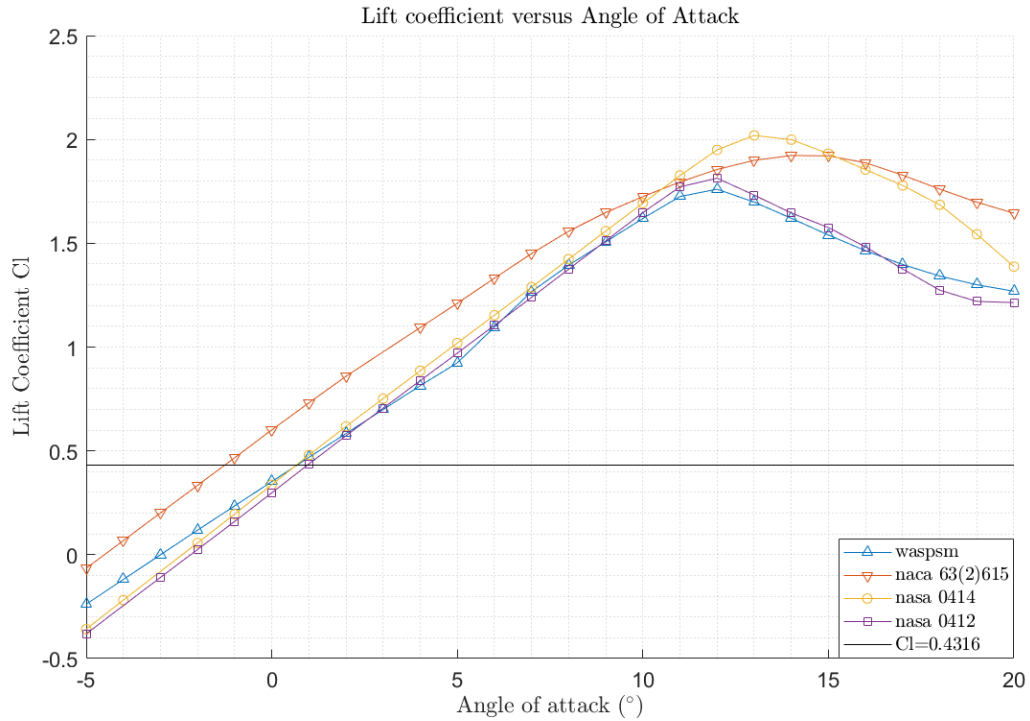
**Figure 4:** Figures (a) and (b).

Figure (a) indicates the Drag Divergence Mach number variation to the thickness to chord ratio for supercritical aerofoils. Figure (b) indicates the variation in the Drag coefficient relative to the Mach number increase, which confirms a better performance of supercritical aerofoils at higher subsonic speeds.

$a_{o,L}$ and the C_{l_a} was taken from the XFOIL data whereas the $C_{l_{MAX}}$ was found using the model suggested by ESDU 84026 for up to 0.4 Mach number and based on that the increment in lift was predicted and therefore the $C_{L_{max}}$ [33].

Thus the NASA 04₂14 has been selected and the sweep angle about the quarter chord of $\Lambda_{c/4}$ has been calculated to be 12°, optimised for cruise gives an leading edge sweep of 30° which based on CFD data is the ideal value for the $L/D = 17.89$ which was initially found for the whole aircraft (Section 14.1.4).

**Figure 5:** Variation of the Lift coefficient versus the angle of attack. It is worth noting that the NACA 63₂015 and the NASA 04₂14 have the highest C_l along with a high stall angle of attack which gives better freedom for take-off and landing.

Taking the values of angle of attack for the Lift coefficient during cruise, the Lift to Drag ratios were compared as shown in the table (1) below for cruise.

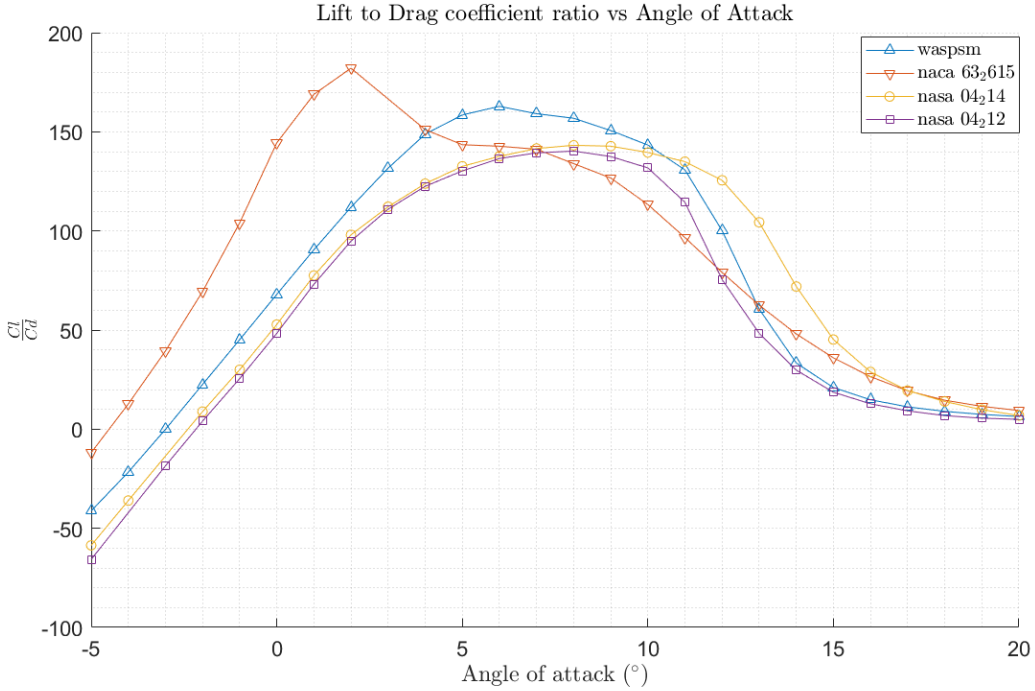


Figure 6: Even though the NACA 63₂015 has the highest C_L/C_d , for the angle of attack during cruise, the highest C_L/C_d can be reached by the waspm aerofoil, followed by the NASA 04₂14.

Table 1: aerofoil characteristics comparison from the graphs.

Aerofoil Name	AoA At Cruise	C_L/C_d	C_{Lmax}	AoA Stall
Wasp Smooth	0.6	81	1.7	12
NASA 04 ₂ 14	0.4	68	1.8	14
NACA 63 ₂ 615	-1.25	65	1.8	15

3.1.5 Thickness To Chord Ratio t/c

A thicker the aerofoil allows more sufficient internal space for fuel, controls, and other systems. Thickness to chord ratio within the range of 12% to 15% can give better C_{Lmax} characteristics. Sufficiently thin aerofoils within the range of 8% to 10% thickness to chord ratio require additional spars or struts to achieve the same stiffness of the structure which makes the wing heavier [1]. However, as shown in Figure 1 and 2a above, when considering compressibility effects over the wing for a subsonic aircraft, a thicker aerofoil will result in lower critical Mach number or Drag Divergence Mach number -in the case of supercritical aerofoils- and therefore in a higher sweep angle, which can have undesirable effects. For the purpose of this design, a compromise was made to the additional weight of the thinner aerofoil with the use of a supercritical aerofoil to achieve the least sweep angle.

3.2 Sweep Angle $\Lambda_{c/4}$

The main direct application of the swept wings except for the increased directional and longitudinal stability is to mitigate the unfavourable effects caused by transonic or supersonic flow over the wing. To determine the sweep angle for the conventional aerofoils such as the NACA 6 series, the critical Mach number where the flow becomes sonic locally was calculated about the quarter chord where the sum of the applied moments and thus C_m can be assumed constant and thus independent of the angle of attack [16] (See Appendix). After applying the sweep angle the new increased $M_{crit,swept}$ will be equal to $\frac{M_{crit}}{\cos(\Lambda_{c/4})}$ which delays the compressibility effects at higher Mach numbers. In the case of the supercritical aerofoils, as mentioned above, the compressibility effects are significant at the Drag Divergence Mach number -calculated in section 14- which is always higher than the M_{crit} and thus less sweep can be achieved.

3.2.1 Effects Of Sweep

Increased sweep reduces the lift curve slope α_s and the maximum lift of the wing. It also causes the boundary layer to be washed out causing unrecoverable rolling moments at the tip and stall. Applied bending moments will be partially

converted into torsional moments requiring an additional torsional stiffening of the wing which will increase the weight. During flight there can be an interaction between the fast period mode and the wing bending mode which can result in flatter.

3.3 Taper Ratio λ

The taper ratio affects the spanwise lift distribution as it is a controlling parameter in the progression of the stall behaviour [1]. If a wing is sharply tapered, there will be a significant reduction in $C_{l_{max}}$ near the tip due to the local reduction of Reynolds number, thus tending to early tip stall. Vortex induced Drag is minimum for a taper ratio of about 0.4 -for unswept wings- as figure (5) shows, but more detailed empirical data described by Egbert Toreenbeck E. [3] show that for business jets at high subsonic speeds the most optimum tapered ratio that will achieve a more linearised induced Drag -i.e linear stable vortices- will be with a taper ratio of 0.38.

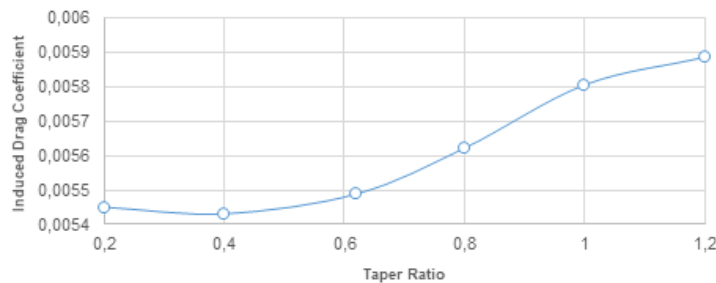


Figure 7: Induced Drag Coefficient variation with taper ratio [7]

3.4 Twist ϵ_t

To delay and prevent tip stall in the case of swept wings, the twist or washout is incorporated in the wing's architecture. Tip stall can occur in an asymmetrical manner causing roll control issues. Twist decreases the aerodynamic loading at the tip, which shifts the center of pressure inboard and thus the wing root bending moment decreases which results in a lower weight. However, twist causes undesirable increased induced drag. Based on empirical data from tables (APPENDIX) for our specific Aspect ratio and sweep angle, the twist was found to be $\epsilon_t = -0.48$ degrees [2].

3.5 Aspect Ratio AR

The Aspect ratio was selected to be equal to 8, which based on empirical data [1] lies within the appropriate range of twin engine transport business jets designed for high subsonic speeds. Due to the 3D effects over the wing, high Aspect Ratio suggests lower induced drag which gives a much less induced tip vortex and therefore more lift is produced and eventually $C_{l_{max}}$ is increased. However, from the Lift to Drag ratio formula (see Appendix) the L/D is proportional to the \sqrt{AR} whereas the wing weight is also proportional to the AR , which means that a higher AR means a heavier wing[1].

After careful analysis of how the AR change from 8 to 9 would affect performance, it was found that the reduction in drag (hence fuel consumption) from the increase in AR was negated by the increase in drag due to the higher structural weight to stiffen the wing. AR of 9 also only reduced the fuel mass by 180Kg but the structural weight increased by $\sqrt{(9/8)} = 106.1\% (\approx 489Kg)$ (from the relation that structural weight $\propto \sqrt{AR}$).

3.6 Dihedral

To avoid extreme stability and lack of manoeuvrability due to the increased stability that the high wing and the aft sweep wings add, negative dihedral -anhedral- is used. Briefly, in high wing configurations a perturbation in the sideslip angle will result in negative rolling moment, in which the aircraft will return to its initial position (dihedral effect). In low wing configurations where this perturbation will result in a destabilising positive rolling moment, the dihedral angle is applied to increase stability and control. Since the lift curve slope of a wing is inversely proportional ($\propto 1/\cos^2(\Lambda_c/4)$) to the sweep angle [2], the effect of the sweep contributes on a lateral stability by an amount equal to 1.21° of dihedral angle -for 12°- [1]. It is worth noting that the combination of high wing and aft sweep configuration prevents excessive spiral instabilities. However, there is an increased tendency for Dutch roll which is encountered by an increase in the vertical tail area which undesirably increases weight and drag. To be able to maneuver and turn and prevent extreme stability phenomena, a wing anhedral of -4° was selected [1].

4 Aerodynamics Analysis - Wing Lift

To transform and construct given the airfoil characteristics the lift distribution on the wing, parameters such as the zero-lift angle of attack, maximum lift coefficient, lift curve slope were determined using empirical formulae [1],[2].

4.1 Zero-Lift Angle Of Attack

The equation for the wing zero-lift angle of attack was obtained according to Raymer as follows[1];

$$a_{0_{L_w}} = \left[a_{0_L} + \frac{\Delta\alpha_0}{\epsilon_t} \right] \frac{\alpha_{0_{LM}}}{\alpha_{0_{LM}=0.3}} \quad (1)$$

where $\frac{\Delta\alpha_0}{\epsilon_t} = -4.08$ describes the change in angle of attack with linear twist and $\frac{\alpha_{0_{LM}}}{\alpha_{0_{LM}=0.3}} = 0.5$ is a Mach number correction factor for cambered airfoils. The exact values were taken from graphs in the Appendix, along with the effect of flaps in the zero-lift angle of attack.

4.2 Maximum Lift Coefficient Of The Wing

The airfoil's maximum C_L is equal to 2.0140, so for operating at within a safe region away from the stall, a maximum lift coefficient of the 2D airfoil of $C_L = 1.8$ was selected. Without considering the effect of the High Lift Devices the 3D maximum C_L on the the wing is given by:

$$C_{L_{max}} = 0.9 \cdot C_{L_{max,airfoil}} \cos(\Lambda_c/4) \quad (2)$$

The sectional increase of C_L caused by flaps is: $\Delta C_{L_{max,airfoil}} = 1.9 \cdot 1.2 = 2.28$ (described in 5.2). The 3D increase in the $C_{L_{max}}$ of the wing is equal to [1];

$$\Delta C_{L_{max}} = 0.9 \cdot \Delta C_{L_{max,airfoil}} \cdot \frac{S_{flapped}}{S_{ref}} \cos(\Lambda_c/4) \quad (3)$$

Thus the final $C_{L_{max}}$ on the wing is given by:

$$C_{L_{max,wing}} = \Delta C_{L_{max}} + C_{L_{max}} \quad (4)$$

4.3 Lift Curve Slope Of The Wing

The wing lift-curve slope was determined using equation in 19.2.5.

Table 2: Aerodynamics-Lift summary data

$\alpha_{0,L}$	$\alpha_{0,L_{flaps}}$	$C_{L_{max}}$	$C_{L_{max}}$ with HLDs	C_{L_α}	C_{L_α} with HLDs
-0.2268	-2.4160	1.58	3.01	0.0731	0.0877

4.3.1 Wing Setting Angle

The wing setting angle was determined as [2]; $i_w = C_{L_{cruise}}/C_{L\alpha_w} + \alpha_{0_{L_w}} = 2.94563^\circ$

5 High Lift Device Selection & Sizing

The key driver in selection of HLDs was the requirement of achieving the chosen design value of $C_{L_{max}} = 3$. Deducting the clean wing maximum lift-coefficient from this value, the required ΔC_L was found to be 1.42. Thus, a HLD which will meet the requirement at lower complexity and drag penalty would be the optimum one.

5.1 Leading Edge Flaps

Leading-edge flaps and slats delay the occurrence of tip-stall and thus increase the lifting characteristics of the wing but they compromise a considerable penalty of additional drag, which is unattractive for efficient cruise and not a necessity if the required C_L for take-off and landing can be achieved only by using trailing edge flaps. As a result, it was deemed not necessary to include leading edge flaps.

5.2 Trailing Edge Flaps

Deflection of the trailing edge flaps reduces the need for higher angles of attack and by giving camber to the airfoil section it postpones the flow separation on the upper surface. To achieve a sufficient take-off and landing lift coefficient, triple slotted flaps were selected. Although during the initial sizing stage, fowler flaps were pre-selected as the maximum landing C_L was selected to be 2.5 rather than 3. Following the poster presentation and the recommendation that the selected wing loading was excessively small, the $C_{L_{max}}$ value was increased to ease the take-off constraint. Fowler flaps also provided a reasonable structural simplicity, nonetheless it would be wiser to sacrifice complexity before performance and safety. Triple slotted flaps offer a significant additional C_L as the additional extension further increases the wing area and therefore increases lift. Moreover, the slotted mechanism allows air to flow from the lower to the upper surface, giving additive lift without an excessive amount of drag. Flaps were assumed to be extended by

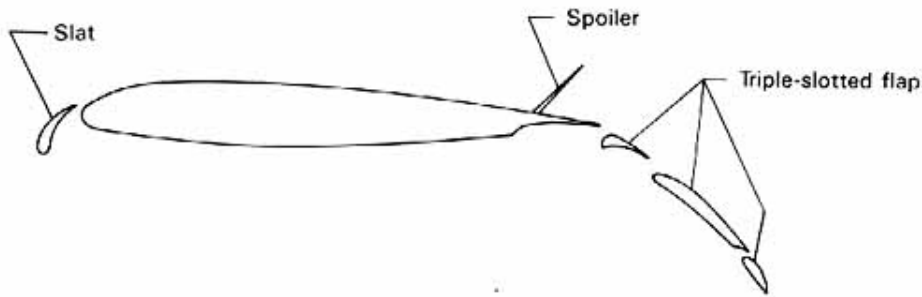


Figure 8: Triple slotted flap configuration,
Image source: <https://history.nasa.gov/SP-468/ch10-5.html>

additionally 20% of the chord, as the 2D $\Delta C_{L_{max}}$ is given by $1.9c'/c$. The flaps' starting point is at a distance of 2.5% of the semi-span away from the root of the fuselage all the way to 75% of the semi-span. The driver for the sizing of the flaps was the required ΔC_L of 1.42. The chord ratio of the flaps was dictated by the aft spar location i.e. at 30% and thus the span ratio needed was calculated based on the flapped area needed.

6 Aircraft System Layout Design

6.1 Fuel System

An aircraft fuel system includes the fuel tanks, fuel lines, fuel pumps, vents, and fuel-management controls. However, the tanks were the only components that impact the overall aircraft layout. Integral fuel tanks (or wet wings) were chosen for structural considerations and as is saved weight and allows the use of areas that would otherwise not be practicable. Integral tanks are cavities within the airframe structure that are sealed to form a fuel tank. The required volume of the fuel tanks was based upon the total required fuel, calculated during the mission sizing. Sufficient space for the fuel tanks was found in the wings, and additional fuel tanks in the fuselage were not required. As the aircraft has high mounted wings, this facilitates the flow of the fuel as it goes directly in the engine without the need of a complex system of fuel pumps and pipes, thus reducing the weight of the aircraft. Another advantage of integral fuel tanks is the proximity to the centre of gravity, meaning there is no large difference between landing and takeoff X_{cg} location. 2216kg of stored in the wings occupied approximately $2.81m^3$ based on the A-1 kerosene density $804kg/m^3$. This was perfectly in line with the available volume $5.15 \times 2.30 \times 0.7 = 8.29m^3$, where 5.15m is the cross section, 2.30m is the mean chord length and 0.3 factor added as a consideration of structural volume in the wing. The volume amount left was utilised by other systems.

6.2 Hydraulic System

Hydraulics in this aircraft has a range of functions with a certain level of redundancy. Hydraulics drive ailerons, elevators, rudders, i.e. flight control surfaces as well as flaps, slats, spoilers and airbrakes, i.e. secondary flight controls. This system is also responsible for auxiliary units, such as the undercarriage, wheel brakes, parking brake and nose wheel steering. A simplified layout below includes accumulators, valve and control cables which make it physically easier to alternate a relative position of a controlled surface. To obtain an immediate response of the

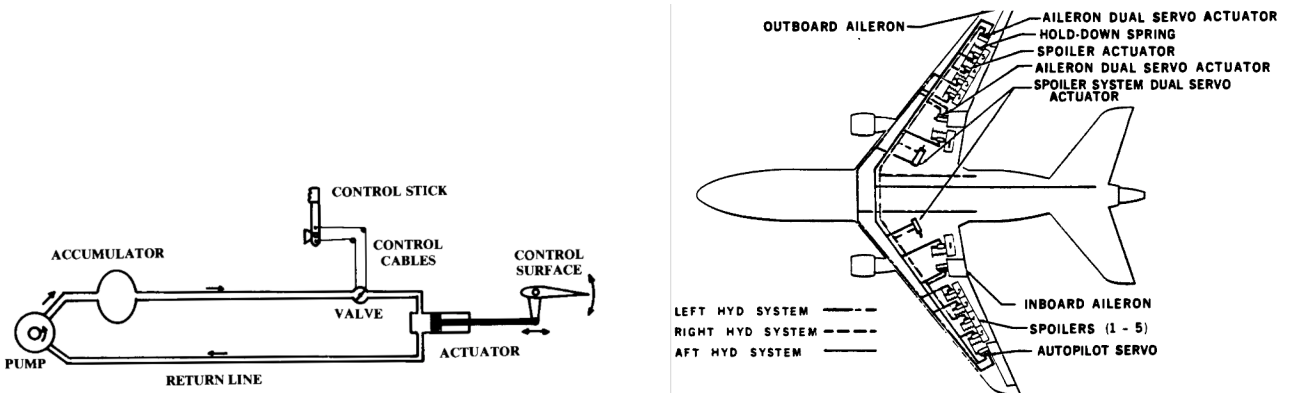


Figure 9: Figures (a) and (b)
Figure (a) Simplified Hydraulics Layout
Figure (b) Actuators Layout

surface, the valve needs to be as close as possible to the actuator. The valve, therefore, cannot be near the cockpit and instead is usually attached to the actuator. The pumps would typically be located next to the engine, in the pylon and the actuator would be close to the control surfaces themselves. The pilot's control inputs are mechanically carried to the actuator by steel cables strung from the control wheel or rudder pedals to the valves on the actuators. It is, therefore, would be desirable to isolate the cables from any physical interaction with other parts. The pilot's inputs are also carried electronically to electro-mechanical valves ("fly-by-wire") to ease the aircraft control during normal operation. The geometry of the fuselage allowed to place the cables and the wires between the fuselage wall and the compartment deck (10cm). This placement utilises space efficiently and protects the cables. To mitigate the effects of water sloshing and ensure the water tanks are equally distant from all control surfaces, the accumulators had to be located closer to the assumed CG location. The placement in the wings above the mid-section of the fuselage was selection, but it decreased the available volume of the fuel tanks. The weight of the wires and tubes are negligible, however, the accumulators can be as big as 500in^3 [14]. For a typical passenger jet ac, a volume of 50 cubic inches is reasonable. From a similar aircraft, a pump supplying 6.8gpm would be sufficient to drive the hydraulics, the dimensions associated are $3.9 \times 4.3 \times 3.8\text{in}$ [15]. Actuators driving primary and secondary control surfaces are located in the wings shown above. Hence the volume taken by the hydraulics without actuators roughly yielded 0.002m^3 .

6.3 Pneumatic System

The pneumatic system provides compressed air for pressurization, environmental control and anti-icing. The system uses pressurized air bled from the engine compressor. Having considered losses associated with the bleed air in Section 8, the air was extracted from multiple compressor stages depending on the operating regime. The environmental systems must provide comfort conditions, i.e. 222°C , $90 - 100\text{kPa}$, and $50 - 70\%$ relative humidity within a closed container (the cabin), under all foreseeable circumstances, i.e. it must provide ventilation, pressurization, heating, cooling, humidification, dehumidification (demisting), and disinfection. One may split air conditioning factors in physical, chemical, and biological. Besides, cabin air monitoring provides the basic smoke detection means for fire warning. A layout shown below takes space in the bottom compartment. A detailed working principle of the air cycle machine can be found in [18]. The requirement for 50pax is 0.3kg/s of air. From [18] the volume occupied by the conditioning systems was found at 1.2m^3 and this was indeed placed in the belly of the aircraft.

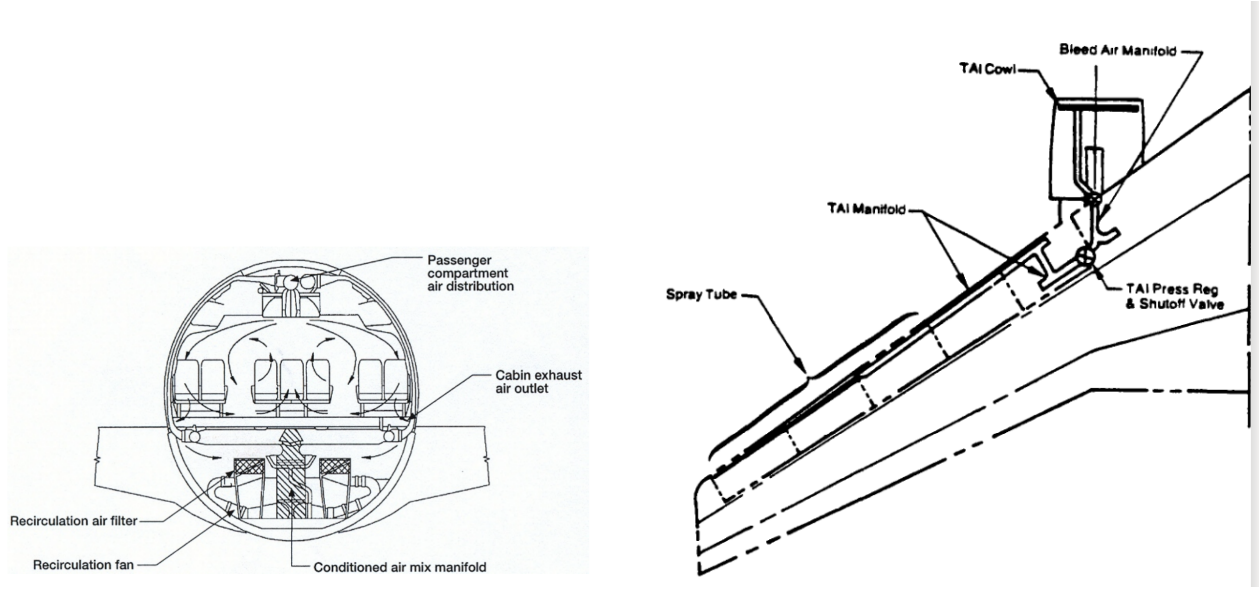


Figure 10: Figures (a) and (b)
 Figure (a) Environmental Systems Layout
 Figure (b) Anti-icing Strip Scheme

Protection against low temperatures in aircraft is needed to avoid ice formation, and to avoid freezing of internal liquids. Having applied propylene glycol to the aircraft on the ground, on a flight through clouds (mainly cumuliform), ice particles and supercooled droplets strike onto frontal surfaces. Generally, a hollow 0.1m wide and 17.4m long strip runs across the wing, providing 210 kW^2 of power to vapour off an ice layer. The same 5.91m strip was placed in the tail-wing. Hence the volume occupied by the anti-icing strips in the main wing was estimated at 0.1347 m^3 . To provide protection against excessive pressure differentials, a positive and negative pressure relief valves were introduced on the fuselage. The cooled compressor air is used for cockpit pressurisation and avionics cooling. Hence two 0.05m diameter ducts were added where the pressurised air travels to and from the engine compressor. These ducts carry the pressurised air to the heat exchanger and supply the clean air to the cabin. The same ducts can be used to use the pressurised air to start on of the engines.

6.4 Electrical System

An aircraft electrical system is a self-contained network of components that generate, transmit, distribute, utilize and store electrical energy. It provides electrical power to the avionics, hydraulics, environmental-control, lighting, and other subsystems. The main component of the Electrical system is the permanent magnet generator which sits on the shaft of the engine. To ensure longer life of the shaft and following the modern trends of the AC generation, the excitation stator and the power stator were introduced. Aircraft generators usually produce alternating current (AC) and are located on or near the engines. For most small and medium-sized aircraft, generation at 28 DC still represents a feasible operating system [23]. From past experience data, a 15kg heavy DC generator located near the engine would be capable of producing 9kW of power. Treating DC generators as back-up sources of electricity, i.e. dividing the lower boundary of electric power requirement from 8 by two, the introduction of 2 such DC generators were sufficient. However, for the reasons of reliability (absence of split commutator rings) and power density AC generators were also introduced to provide the required redundancy of the electric system. From [23] the typical power density would vary from 0.66 kV a/kg and 1.33 kV a/kg (taking average further in the calculations). Because two engines should be capable of producing at least 50kW each and assuming power factor of 0.9 the aircraft needs to take an additional 110kg of weight. From [24], it was calculated that the weight of wires is equal to 32 grams per kilogram payload. Hence the wire weight is approximately equal to 175kg. These value correlate with the weight values in Section 7. Both generators were located in the engine pods such that the volume of the fuel tanks was not reduced. The location there also allowed for safe cooling, reducing the chance of an emergency in the case of overheating, making the design of the pylons more complicated.

6.4.1 More Electrical Aircraft (MEA)

Since the beginning of our project, one of the main concerns was the environmental impact of the aircraft, this explain the choice to adopt the MEA concept which revolves around the idea of replacing most of the aircraft secondary systems, currently operated by mechanical, hydraulic and pneumatic power, with systems powered by electricity. The

MEA offers improved power system efficiency, reliability and maintainability, while reducing the weight and volume of the subsystems. This will lead to lower fuel consumption, lower emissions and reduced total cost. Following the examples of the B787 and A380, the commonly used Integrated Drive Generators (IDGs) will be replaced by Variable Frequency Generators (VFGs) directly coupled to the engines. This innovative architecture does not require complex hydro-mechanical IDG, DC-links, cycloconverters or other switching, thus improving the reliability of our system.

6.4.2 Auxiliary Power Unit (APU)

As Aircraft batteries might last only 30 minutes, most commercial aircraft use a jet-fuel APU. Usually, an APU is designed to provide ground power for air conditioning, cabin lighting, and engine starting. This device frees the aircraft from any dependence upon ground power carts. The APU is also used for in-flight emergency power, and in some cases is run continuously in-flight for additional hydraulic and electrical power. The APU requires inlet and exhaust ducts and have high maintenance requirements, so access is important. The exhaust of an APU is hot and noisy and therefore is preferred to be placed in the tail section for commercial aircraft as shown in the picture below. By looking at typical aircrafts the volume of the APU was found to be $0.4m^3$. From looking at the fuselage tail design and at the APU's dimensions for similar aircraft, it is concluded that there is sufficient volume to place the APU in the tail.

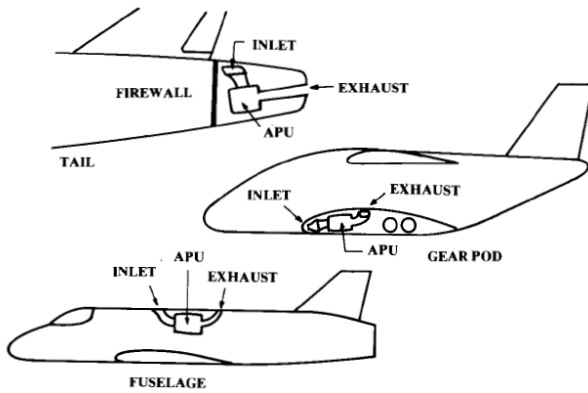


Figure 11: APU Installation (Raymer)

6.5 Actuators

Actuators in aircraft play a key role in flight and control. Their operation ensures the safety of the plane and every passenger on board. In commercial aviation, actuators are used in landing gear and flaps. In recent years, engineers have developed the Electro-Hydrostatic Actuator (EHA), which combine electrical and hydraulic power following the MEA concept. EHAs are electrically powered but use small hydraulic pumps and reservoirs that transform electrical energy into hydraulic power, as shown below. They allow designers to segregate power distribution channels and save weight efficiently. The picture below represents the position of the actuators in the wings (the same layout was adopted for the tail-wing). From [25], the typical volume occupancy of the actuators system is about $0.04m^3$. The actuators were indeed placed in the main and the tail wings, to ensure immediate response of the surfaces.

6.6 Avionics

Avionics includes radios, flight instruments, navigational aids, flight control computers, radar, and other aircraft sensors such as infrared detectors. The radar is normally held in the nose of the aircraft. Transport-aircraft radars are only for weather avoidance, thus they are small relative to the size of the aircraft nose, and a length of 0.5m is sufficient for this aircraft. Usually, avionics has a density of about 481-720 Kg/m³. Using empirical data, the uninstalled avionics weight is estimated at 220kg. Therefore, taking an average density of 600kg/m³, avionics volume is around $0.36m^3$.

7 Weight & Balance Predictions

In the initial sizing of the conceptual design, weights were estimated based on mission profile and design specifications. The obtained results are shown in Section 1. In this section, weights for every component will be estimated using physics based, augmented by empirical corrections equations provided in [31]. Using the overall layout of the aircraft and the formulas to estimate component CG provided in [31], components' locations were estimated. Having the center of gravity location and weight for every component, the aircraft center of gravity was estimated using the

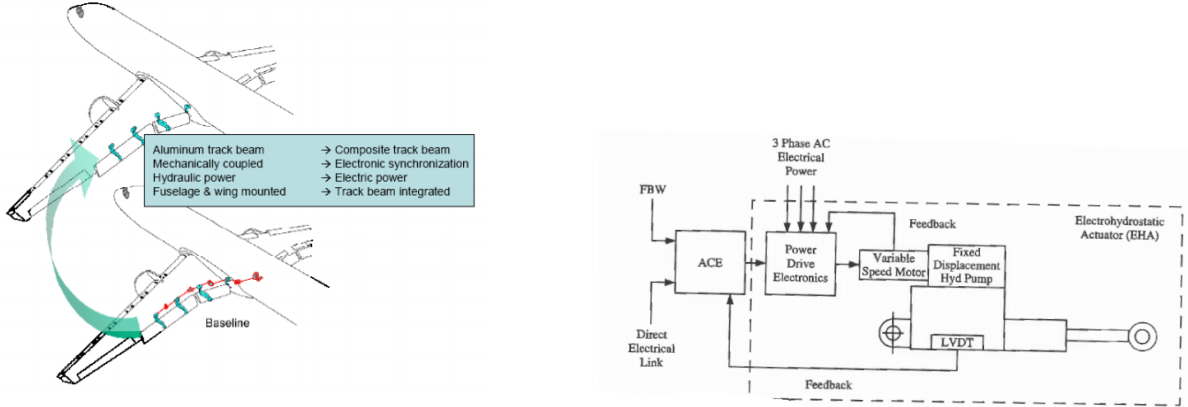


Figure 12: Figures (a) and (b)
 Figure (a) Actuators In The Wing
 Figure (b) Electro-Hydrostatic Actuator Layout

formula provided in [31]. The obtained results are presented in the table below, where the x-locations are measured from the nose of the aircraft, and the z-locations from the center line of the fuselage. As the aircraft have the weights evenly distributed in the lateral direction, it was not required to calculate the y-component of the centre of gravity as it will be zero.

Table 3: Weight breakdown for the aircraft

Weight Breakdown			
Airplane Type: Regional Jet Aircraft		Date: 21/11/2019	
Engine Type: 2 Turbofans		Name: Group 21	
Components	Weight (Kg)	x (m)	z (m)
Wings	711.8	2.20	1.60
Horizontal Tailplane	62.2*	22.50	4.01
Vertical Tailplane	61.3*	21.14	2.92
Fuselage	2029.2**	9.78	0.00
Main Landing Gear	460.7	11.70	-1.30
Nose Landing Gear	113.5	2.90	-1.30
Nacelle	198.6	12.20	0.00
Engine Controls	28.4	12.20	0.00
Engine (Pneumatic) Starter	38.6	12.20	0.00
Fuel System	33.8	12.20	1.60
Flight Controls	238.1	1.00	-0.30
Installed APU	228.0	21.50	0.40
Instruments	99.1	1.50	0.00
Hydraulic System	46.6	12.00	0.60
Electrical System	321.9	12.20	0.00
Avionics	219.7	1.50	0.00
Furnishings	1061.3	12.00	-0.30
Air-Conditioning	261.8	13.00	1.50
Anti-Icing System	31.2	11.70	1.60
Handling Gear	4.6	1.00	-0.30
Engine And Contents	1849.4	12.20	0.00
Empty Weight	7988.8	11.11	0.13
Passengers	3775.0	11.00	0.00
Crew	400.0	3.50	0.00
Overhead Bags	200.0	12.50	1.40
Luggage	800.0	10.0	-1.10
Galley	150.0	18.25	0.30
Fuel	2216.0	12.20	1.60
MTOW	15530.0	11.10	0.40

(*the tail weight was reduced by 25% thanks to the use of composites; **the fuselage weight was reduced by 15%

thanks to the use of composites).

These results were obtained by applying an iterative process, changing the location of different components such that stability at different loading conditions (MTOW, MZF,...) was not affected, while considering our constraints in the placement of each component. This will be explained in more details in Section 14. The weights and centre of gravity locations at different configurations were then plotted in Figure 13 to know the range of horizontal cg movement.

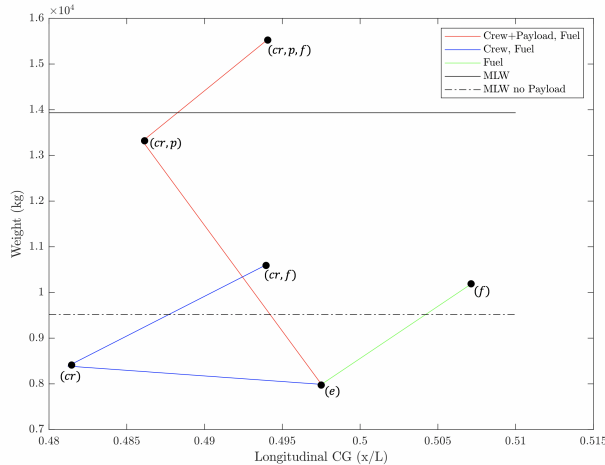


Figure 13: Range of horizontal center of gravity movement

8 Powerplant Selection, Installation & Integration

8.1 Uninstalled Thrust

Environmental impacts drove the selection process of a powerplant. Although podded engine have higher wetted area than buried engines they offer substantial advantages that have made it standard for commercial and business jets. Podded engines place the inlet away from the fuselage, providing undisturbed air with a very short inlet duct. Podded engines produce less noise in the cabin because the engine and exhaust are away from the fuselage. By looking at the engines of similar aircraft, cruising at similar altitudes and speed CF-34 was selected. From the engine manual, the scaled SFC value for cruise and minimum drag operations provided by the manufacturer yielded 10.5mg/Ns and 9.50mg/Ns respectively [21]. Having changed the constraint calculations, the overall weight yielded 15,590 kg, and the thrust to weight ratio was calculated to be 0.36. This ratio led to 53,150 N of thrust required at sea-level. However, this value does not account thrust losses due to installation of the power plant. The losses are due to nacelles imperfect pressure recovery, bleed air and power extraction.

Inlet and nozzle external losses can be expressed as a fraction of uninstalled thrust T, so that

$$T = F - \phi_{inlet}F - \phi_{nozzle}F \quad (5)$$

where $\phi_{inlet} = D_{inlet}/F$ and $\phi_{nozzle} = D_{nozzle}/F$ [19]. Since the shelf engine had to be selected, as designers we cannot alter the nozzle but can create an optimal inlet. Hence it can be assumed that ϕ_{nozzle} is negligible and the uninstalled thrust becomes the function ϕ_{inlet} only. Now, we know that the typical Mach Number at the throat lies within 0.5 to 0.6. From (14) it can be seen that for $M_0 = 0$ ϕ_{inlet} becomes large. This makes sense, as during takeoff the air is sucked from behind the "lip" and the accompanying adverse pressure gradient make boundary layer separation a constant danger, in which the additive drag will not be regenerated. Hence it can be deduced that at $M_0 = 0$ $\phi_{inlet} = 0.075$.

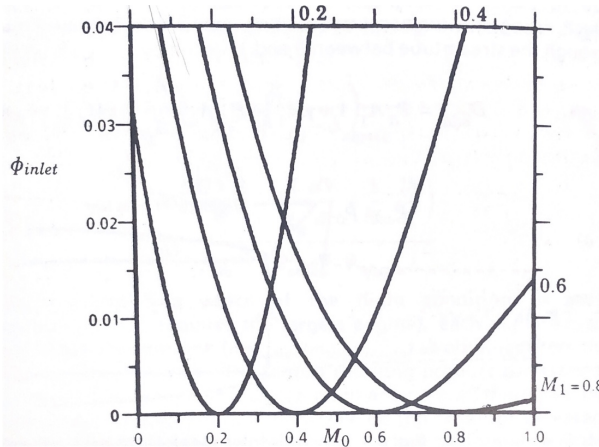


Figure 14: Additive Drag Factor against Mach Number

For altitudes 30000 ft and 40000 ft reductions of 6 percent can be shown for maximum bleeds if FTIT is exceeded. Typically the value of bleed losses is about 0.2% for cruise [21]. Typically electrical equipment consumes around 50 kW 200 kW which converts to 1000 N extra thrust. So, to calculate the installed thrust F the following equation can be used:

$$(F - F \times 0.06 - 1000) \times (1 - \phi_{nacelle}) = 53150 \quad (6)$$

which leads to $F = 62,191$ N. A single CF-34 engine produces 35,500 N making it reasonable to scale the engine down slightly using rubber engine approach. $L = L_{actual} \times (SF)^{0.4}$, $D = D_{actual} \times (SF)^{0.5}$, $W = W_{actual} \times (SF)^{1.1}$ where $SF = 0.926$, $L_{actual} = 2.60m$, $D_{actual} = 1.20m$, $W_{actual} = 760kg$. Hence the rubbed engine has the following dimensions: $L = 2.47m$, $D = 1.1m$, $W = 625kg$ (excluding nacelle and thrust reversers).

8.2 Nacelle Design

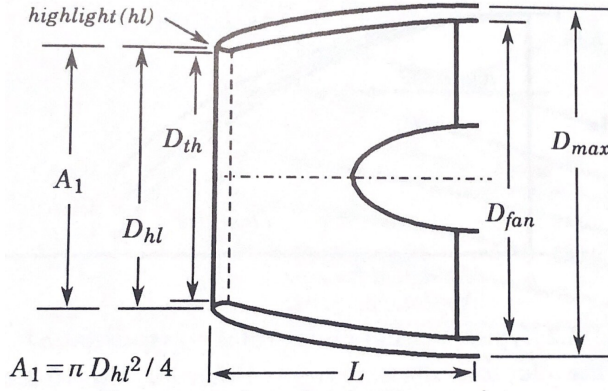


Figure 15: Nacelle Layout

Calculations of additive drag are interconnected with the nacelle design. The diameter at the throat of the subsonic inlet is sized such that the Mach number does not exceed 0.8. This provides some margin for growth since one-dimensional Mach number at the throat corresponding to actual inlet choke is about 0.9. The diameter can be calculated using

$$D_{th} = \sqrt{\frac{4}{\pi} A_{th,max}} = \sqrt{\frac{4}{\pi} \left(\frac{m_0 \sqrt{T_{t0}}}{P_{t0}} \right)_{max} \frac{1}{MFP@M = 0.75}} = \sqrt{\frac{4}{\pi} \frac{\sqrt{518.7}}{2116} \frac{m_{c0,max}}{MFP@M = 0.75}} \quad (7)$$

and reduces to

$$D_{th} = 0.1636 \sqrt{m_{c0,max}} \quad (8)$$

where $m_{c0,max}$ has units lbm/s and D_{th} has units of feet. From the unscaled flow rate value provided by the manufacturer ($m_{c0,max} = 200kg/s$), D_{th} yielded 1.05m. Scaled the airflow D_{th} yielded 0.954m. Using Figure 15, the D_{hl}/D_{max} could

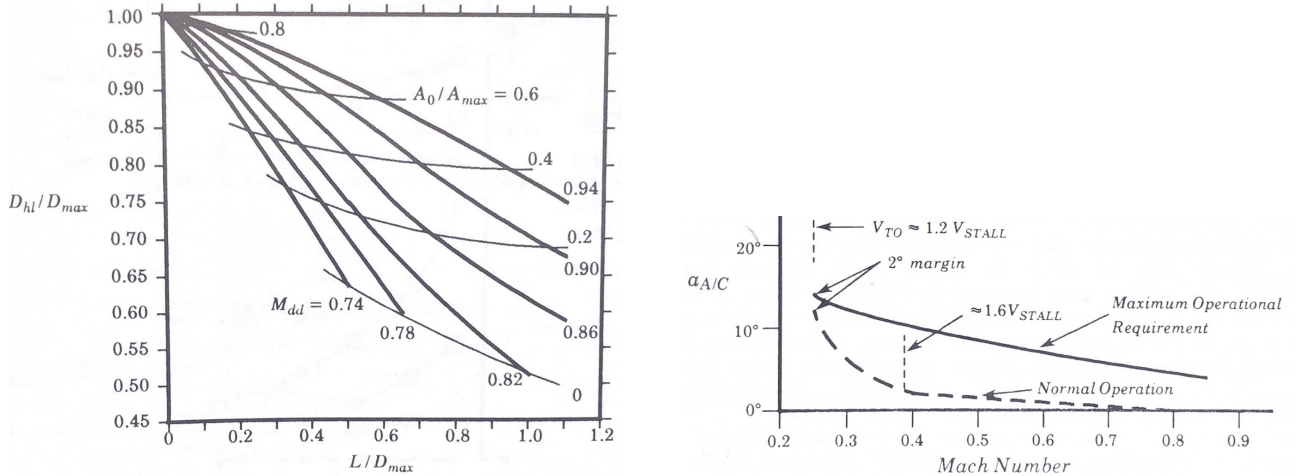
**Figure 16:** Figures (a) and (b)Figure (a) Diameter Ratio against Length For Different M_{dd}

Figure (b) Angle of Attack Variation

be reasonably approximated as D_{th}/D_{fan} as the thickness of the nacelle was small (approximately 3cm thick according to Raymer) compared to the fan radius, i.e. $D_{max} \approx D_{fan}$. Thus, for the calculated $M_{dd} = 0.75$ and $D_{th}/D_{fan} = 0.87$ the NACA 1-Series Contour required $L/D_{max} = 0.27$ where L is the length of the nacelle. Thus the the length of the nacelle was estimated to be 0.3 meters. During aircraft's flight angle of attack can vary substantially, which change the angle of the air flow with respect to the centreline of the engine. These variations normally occur during landing and takeoff rotations. Figure 16 b displays change in angle of attack for a typical subsonic passenger aircraft. The most significant variations occur between $1.2V_{STALL}$ and $1.6V_{STALL}$. Inclining the face of the nacelle can compensate for these variations. The incidence of the nacelle face can be calculated using

$$\alpha_{nac} = 0.5^\circ + 1.4\alpha_{A/C} \quad (9)$$

where $\alpha_{A/C}$ is the cruise angle of attack for the aircraft. A compromise between the 2000 km cruise optimisation, loiter and the second cruise lead to $\alpha_{nac} = 3^\circ$. The effect of the crosswind can be reduced by making the leading edges on the side on the inlet thicker to minimise probability of the flow separation. To suppress the yaw moments due to the engine blades rotations , the engines were rotated by 2° towards the fuselage. Although the thrust reversals add mass, i.e. 30% of the nacelle weight they significantly help on slippery runways and reduce brake wears [32].

8.3 Engine Location And Pylons

The relative location of the engine depends on the wing design and the dimensions of the engine. If the engine had been located close to the engine it would have ingested a vortex off the fuselage or a separated wake from the wing stalling the engine, hence the engine was located one diameter away, i.e. 3.2m from the fuselage (measuring from the edge of the nacelle). The engines intakes had to be placed in front of the leading edge of the wing such that the disruption of the flow is minimal. By looking at similar aircrafts, it was noticed that the engines are moved forward such that the start of the nozzle of the engine can be seen from the top view. Taking into consideration sweep angle @ $c/4$ to be equal to 12° and the engine length to be 2.47m the centreline intake distance from the leading edge yielded 2.35m including the nacelle. Additionally, the thickness of the pylon t was required for the drag calculation. Thickness of the pylon is a structural parameter and was predicted to be 15cm. To achieve a desired trimmability and ensure minimal interaction of the exhaust and the deployed HLDs, the engine was required to be moved downwards, towards the centreline of the fuselage by 70cm. The latter value was found from the vertical displacement of the 3-slotted HLDs at maximum deflection angle during landing. This effect was also favourable from the undercarriage point of view as it pushed the CG location closer to the ground.

9 Undercarriage

9.1 Constraints And Strut Loads

From the moment balance about the nose of the fuselage and the force equilibrium:

$$W_0x_{cg} - W_{mg}x_{mg} - W_{ng}x_{ng} = 0 \quad (10)$$

it can be shown that:

$$\frac{W_{ng}}{W_0} = \frac{x_{mg} - x_{cg}}{x_{mg} - x_{ng}} \quad (11)$$

This ratio is an important indication of the load distribution between the nose and main undercarriage. To ensure that an aeroplane has sufficient steering capability, this ratio has to be larger than 0.05. At the same time, having this ratio larger than 0.2 would imply an over-designed and bulky nose landing gear. Having assumed the centre of gravity of the aircraft at takeoff at $x_{cg} = 10.76$ and $z_{cg} = 0.25$ the nose gear and the main gear were placed at $(x, y) = (2.9, 0.0)$ and $(x, y) = (11.7, -1.33)$ from the nose respectively. After several iterations, the height of the strut was chosen to be 0.45m (described below). The number of wheels was selected to be 2 per each strut with three struts in total (two for the main gear and one for the nose gear). The load on each strut of the main gear was directly calculated from 11 and was estimated to be 44.5% of the total weight.

The advantage of the high-mounted wing is that the clearance constraint put on the lateral location of the main gear is satisfied, i.e. the vertical distance between the tip of the engine and the 5 degrees line running from the outermost contact point of the main gear is almost always greater than 6 inches.

To avoid a tail strike an angle between the ground and the line connecting the aft-most lowest part of the fuselage with the contact point of the main gear, i.e. tip back angle had to be considered. The tip back angle during landing or takeoff rotation has to be greater than lift-off angle of attack (9°) and smaller than the angle between the vertical height and the line connecting the contact point with the centre of gravity (82.35°). Note, however, that the tip back angle could only be calculated after the tyres had been selected. The angle was found to be 16.4° .

To avoid overturning in sharp turns, the overturn angle shown below had to be greater than 63° and was estimated to be 62.9° . The angle is between the vertical distance between the lines connecting main and nose gear and the parallel line passing through the CG and the horizontal distance connecting the same two lines [35]. This criterion was our stumbling block, and big compromises were made at this stage. The disadvantage of the high-wing aircraft is that its vertical CG is high above the ground and the lateral position of the main gear is constrained by the diameter of the fuselage. This combination makes an aircraft laterally unstable on the ground and less suitable for cross-wind landing. For this reason the gear struts were moved further towards the side edge of the fuselage. Keeping the strut length the same and moving the wheels to the edge would mean that during landing when oleos deflect the tires most certainly strike the fuselage skin. Increasing the length of the strut while moving them to the fuselage edge would mean that a complex folding mechanism would have to be introduced for which the analytical tool was not provided. Therefore, an underbelly pod was added, which would ensure the lengths of the struts stay small, and the oleo deflection during landing does not damage the fuselage. This indeed increased the drag penalty during cruise operations.

9.2 Tire Selection

To find the load applied to each wheel of each main gear strut the following formula was used:

$$W_W = \frac{L_{static} \times 1.07}{N_{wheels}} = \frac{63534 \times 1.07}{2} = 36520N \quad (12)$$

where 1.07 is a statutory safety factor. The static nose gear load was estimated to be 16413N However, the nose gear is also subject to dynamic loads that can be even more significant. These loads are the direct results of the compression on the nose gear that came from the inertial moment imparted on it during deceleration. The following formula from [1] was applied:

$$W_{dynamic,noseu/c} = \frac{10HW_0}{gB} = \frac{10 \times 2.65 \times 14835}{9.81 \times 9.2} = 12038N \quad (13)$$

for an assumed deceleration of $10ft/s^2$ where H is the aircraft CG height above the ground, $B = x_{mg} - x_{ng}$ and W_0 is the aircraft weight. The largest dynamic load would be imparted on the strut during an aborted takeoff. Hence, when calculating nose gear loading the maximum between the static and dynamic had to be considered. Thus using the same formula above the nose gear tyre load was estimated as 8781N. Based on the estimated loads $18 \times 5.7 - 8$ tyres were selected for the main gear and $13.5 \times 6.0 - 4$ for the main gear [11]. The aim here was to choose the smallest possible main gear tyres to minimise the size of the extended undercarriage box.

9.3 ACN Estimation

Having chosen tyres, it was then crucial to check if the undercarriage configuration was suitable for runways. The majority of airports according to [9] have asphalt runways therefore the ACN number was compared against Flexible PCN Number. The output ACN number NUMBER was lower than typical values of PCN associated with various runways at different airports, such as JFK Runway 4R/22L PCN = 90, Heathrow Runway 09L PCN = 83, KLAX Runway 7R/25L PCN = 75 and KLAS Runway 8R/26L PCN = 100 [10]. If an ACN is lower than PCN of a runway then an aircraft is suitable to operate on such runway.

SG	CBR	Flex t, in	ACN Flex	k, lbs/in^3	Rig t, in	ACN Rig
D	3.0	16.97	6.6	73.7	5.67	7.8
C	6.0	11.59	6.5	147.4	5.40	7.6
B	10.0	8.73	6.5	294.7	5.13	7.5
A	15.0	6.88	6.6	552.6	4.94	7.5

Figure 17: ACN For Different Runways

9.4 Oleo Sizing

The purpose of a shock absorber is to convert vertical Kinetic Energy into motion of a damped stroke and also to absorb some of the energy in the form of compressing air/ fluid when significant loads are applied. The most common type of shock absorber is the oleo-pneumatic strut shown in [36]. It has two main chambers, the bottom chamber filled with viscous liquid and the top chamber typically filled with oxygen or nitrogen. The piston moves upwards as the load is applied to it, and the oil moves from one chamber to the other through a small orifice.

Relating the Kinetic Energy of the aircraft to work done by shock absorber:

$$\frac{W_{landing} V_v^2}{2g} = (\eta LS)_{shockabsorber} + (\eta_T LS_T)_{tire} \quad (14)$$

where $V_v = 10 ft/m^2$ is vertical speed which is specified by FAR 25, $\eta = 0.85$ is the efficiency of a typical modern shock absorber, $\eta_T = 0.47$ is the tire efficiency ratio, L is the average total load on the shock absorber during deflection, S_T is the stroke of a tire and S is the stroke of the shock absorber. The tire stroke assuming that the tire deflects to its rolling radius is equal to half a diameter minus the rolling radius, i.e. $S_T = (18.5/2 - 7.55) * 0.0254 = 0.0432m$. The shock absorber and the tire act to decelerate the aircraft from the vertical landing velocity to zero vertical velocity. The vertical deceleration rate is called the "gear load factor" (N_{gear}). $N_{gear} = L/W_{landing}$ and is typically equal to 3 for general aviation. Hence, rearranging for S from (14):

$$S = \frac{V_v^2}{2g\eta N_g} - \frac{\eta_T}{\eta} S_T = \frac{3.05^2}{2 \times 9.81 \times 0.85 \times 3} - \frac{0.47}{0.85} * 0.0432 = 0.1782m \quad (15)$$

The stroke calculated by (15) should be increased by 1 inch as a safety margin. Airworthiness dictates that the stroke of the shock absorber is directly related to the static oleo deflection, where the deflection = $\frac{2}{3}S$. This ratio is based on the internal pressure of the air or nitrogen chamber. Hence the strut height had to be at least 2.5 of the stroke, i.e. $0.45m$.

For the purposes of drag calculations, considering a typical internal pressure, the diameter of the main gear oleo-pneumatic strut could be estimated as follows [1]:

$$D_{oleo_{mg}} = 0.04\sqrt{L_{oleo}} = 0.178m \quad (16)$$

where L is the maximum load applied on the oleo in pounds and diameter D is given in inches. For the nose gear L_{oleo} is the sum of dynamic and static loads where $D_{oleo_{ng}} = 0.0812m$.

9.5 Retraction Mechanism And Discussion

When choosing the dimensions and the location of the main gear, it was crucial to consider two things: whether the tires stroke the fuselage during landing and whether the gear could be fully retracted in the fuselage without 1) obstructing each other and 2) touching the cabin deck when fully retracted. Moving the struts to far off the centre line almost guaranteed gear striking the fuselage (for the same oleo length), moving too close would increase the overturn angle, enforcing complex folding retraction mechanism.

The lateral dimension was fixed at 133 cm from the central line to satisfy the overturn angle criteria. The minimum height between the ground and the fuselage was estimated to be half of the wheel dimension plus the deflection of the oleo. This ensured that the wheels did not strike the fuselage during landing. Hence, the minimum ground clearance was $h_{clearance} = 18.5 * 0.0254/2 + 0.12 = 0.35m$. From the dimensions of the fuselage, it became clear that a pod undercarriage box had to be introduced to ensure full retraction of the gear. This compromise was indeed expected at an earlier stage of the design as high-mounted wings do not provide the extra volume where a part of an oleo can be located. The width of each wheel is 15.24cm, and the minimum gap between the wheels is approximately 12.6cm (strut width) plus 5cm gap between the wheel and the strut. Hence 45cm of the overall strut height is required to accommodate the retracted wheels at 21° relative to the horizontal line. The weight of one wheel is 6.3kg [12]. From [13], it is known that undercarriage struts are usually made of β phase Titanium (Ti-10V-2Fe-3Al) which has a density of 4650kg/m³. Although the strut has empty volume and oil in the absorbers, it would be reasonable to assume 0.90 of the strut consists of titanium. Hence $M_{strut_{mg}} = \pi \times \frac{D_{oleo_{mg}}}{4}^2 \times H \times \rho_{Ti} = 46.8kg$ and $M_{strut_{ng}} = 9.76kg$. The retraction hinge was assumed to be ideal and the corners of the strut were assumed to be small at the hinge.

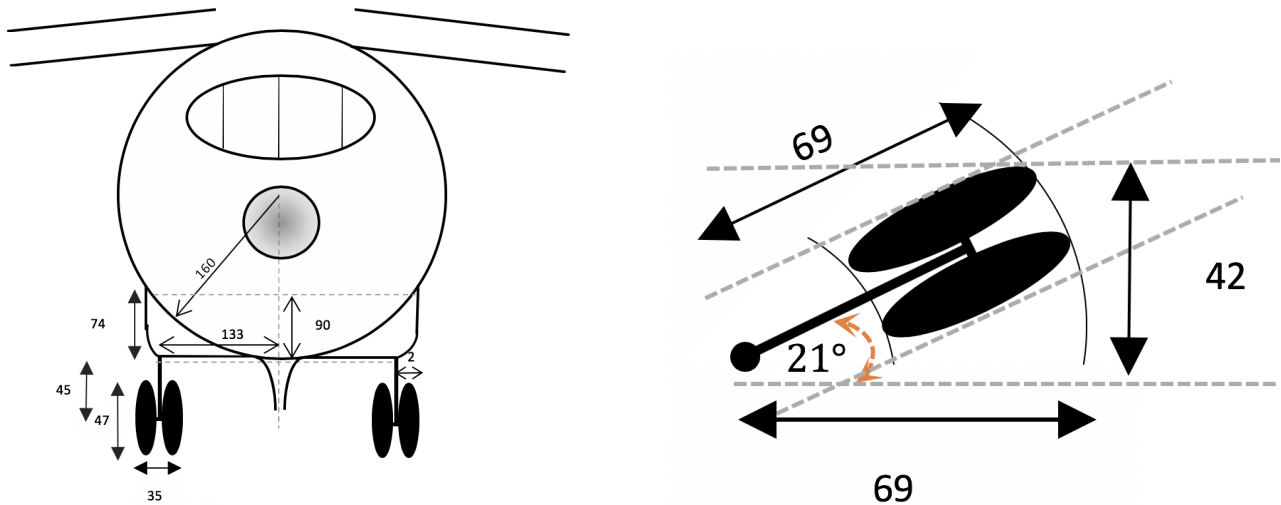


Figure 18: Figures (a) and (b)
Figure (a) Main Gear Dimensions
Figure (b) Retraction System

10 Structural Layout

When considering the structural layout, the main objectives were i) utilisation of span loading to ensure that opposing loads act near each-other to reduce weight and sizing of the structural members ii) provision of efficient load-paths and transferring loads between members effectively iii) complying the FAR 25 requirement of having a fail safe design to control failure of other components if one fails iv) having multi-function components for weight reduction.

10.1 Wings

FAR 25 requires that the engine supporting structure should withstand a limit engine torque imposed by sudden engine failure or maximum engine thrust. Moreover, several loads such as lift, drag and weight forces all act through the wing. Therefore, the wings are required to be strong and stiff to withstand high bending, torsional and shearing stresses. The forward spar at 20% chord and aft spar at 70% chord will be running along the span. Spars will carry the bending stresses on the wings. The forward position is selected to maximise the fuel storage capacity of the wings whereas the aft spar position is dictated by the HLD placement and their required chord ratio. Selecting the aileron and flaps chord-ratio to be the same allowed the spars to also be used as the point about which both the flaps and ailerons rotate. This multi functionality meant that structural weight can be minimised.

Ribs are placed in the wings to maintain the aerodynamic shape. Heavy ribs will also be placed on the engine attachment points to provide sufficient support. Heavy ribs will also be used around the fuel tanks which will run between the front and aft spars. Bulk heads will also be placed in the wings to divide the fuel tank.

The engines are chosen to be placed on the wings as they are crucial for span-loading i.e they increase the weight opposing the lift forces, thus reducing bending stresses/strains on the wings. The engines are attached to the wings on pylons, which ensures a fail-safe design in the unfortunate case an engine catches fire or gets struck by a bird. The skin, which will include stringers to prevent buckling, is used to enforce the wing by carrying shear and pressure loads. Structural consideration was also a key driver in the decision to minimise sweep. This is because sweep increases the load transfer distance and it moves the aerodynamic centre back, introducing torsional loads on the wing. This would have led to larger reinforcement such as spars and also a thicker/stronger skin to carry the torsional loads.

To realise a straight uninterrupted load path and also a sufficient room inside the cabin, the wings are placed outside of the fuselage in a pod. Although this comes at the cost of extra-drag (due to larger wetted area), the benefits are i) higher integrity of the wings and the fuselage as interruptions are minimised and load is transferred directly ii) placing the wings outside prevents an increase in diameter of the fuselage by around 20-30 cm and hence reducing drag and weight.

Spars and ribs are chosen to be made from aluminium-alloy due to the high specific strength stiffness, light weight, inexpensive and easy to machine. A metallic skin (possibly an aluminium alloy combined with other metals such as zinc, magnesium etc) is selected as increased corrosion resistance, indentation resistant and strength are the key drivers. The HLDs and ailerons will be made from composites for weight reduction.

10.2 Tailplane

The tail-plane (both horizontal and vertical) will have two spars located at 20% and 70%. Again the placement of aft spar is dictated by the elevator and rudder sizing required where as front spar is selected to minimise bending stresses near the leading edge. Ribs and skin, similar to the wings, will also be used to strengthen the structures. Larger ribs are placed at the interface between the vertical and horizontal tail for reinforcements. The tail is chosen to be made of CFRP to reduce structural weight whilst also meeting the.

10.3 Fuselage

Large number of stringers will run along the fuselage especially around the cut-out areas to carry bending. The main cut out areas are the cabin and emergency doors, under-belly cargo door and the front and main landing-gear housings. Weight is minimised when stringers run uninterrupted and thus minimising cut-outs was a key driver. Since stresses are the greatest on the fuselage around the vicinity of the wing, it was advised that cut-outs should not be placed in this region if possible.

Frames are placed near the cargo, undercarriage, wing and tail mountings to enforce the fuselage structure by carrying shear loads. FAR 25 also requires the fuselage to be strong enough to carry flight loads plus pressurisation loads from zero up to the maximum release valve setting[27]. Hence, bulk heads will be used to carry pressurisation loads and separate the pressurised vessels from the tail. The fuselage skin and floor panels are made from composites whereas the frames, stringers and bulk-heads will be aluminium alloys or other metallic alloys to ensure they can carry stress in different directions.

10.4 Landing-Gear

The landing gear attachment in the fuselage belly is driven by the need for multiple load paths for a fail-safe design. Thus the struts of the landing gears should not be attached to a single frame but rather multiple if possible, thus it was made sure that sufficient area is provided before and after the landing gear attachment point for the frames to be implemented. The landing gear is to be made of steel alloy due to the high strength and fatigue resistance at the desired temperatures.

10.5 Aero-elastic Effects

To minimise the effects of wing flexing, the AR of the wing should be reduced. Since the selected AR is not excessive i.e. wing is not prone to flexing hence the stiffness of the wing didn't need to be increased. Thus, during the wing design, it was necessary to consider the structural aspects of how AR affects the possibility of aileron reversals occurring. Mass balancing will also be used to reduce control surface flutter by placing lead in the leading edge of control surfaces.

11 Tailplane Sizing And Design

The tail-plane's main purpose is to ensure that the aircraft is controllable, trimmable and stable (both statically and dynamically). The tail must be sized such that all the above requirements could be achieved at any operational condition within its flight envelope and at the most extreme centre of gravity positions.

The T-tail is selected for this design project mainly to reduce the interference with the wake of the wing, which in-turn is driven by the high-wing configuration selected. Placing the horizontal stabiliser over the vertical stabiliser aims to ensure that the flow over the tail is not affected by the wings, fuselage or engines. Therefore, the T-tail reduces the losses in pressure and hence increases the tail efficiency η_H , which is defined as the ratio of dynamic pressures over the tail to that of the wing. Generally, the efficiency of the T-tail is taken to be approximately 1. Due to this increased efficiency, the tail size required could be smaller when compared to other configurations. Smaller area is desirable for drag reduction. The lack of wing-tip for the vertical stabiliser also means that trailing vortices don't form on the vertical surface and thus higher lift could be generated for a given surface area, this phenomenon is called the 'end-plate' effect.

Correctly designing, sizing and positioning the T-tail was key to ensure it meets all the controllability, stability and trimmability requirements. This process was iterative as it depended on the position of the wing, centre of gravity, aerodynamic efficiency of the wing and fuselage effects (which depends on fuselage size and shape). Hence, the positioning of the tail from the wing and the area of the vertical and horizontal tails was optimised.

11.1 Horizontal Tailplane

A fixed horizontal-tail with an elevator mounted on the trailing edge, is selected to provide longitudinal trim, controllability and stability.

11.1.1 Disposition

Generally, the vertical position of the horizontal-tail is constrained by post-stall behaviour of the aircraft and the stability requirements, i.e. $\frac{dC_m}{da} < 0$ at and after stall. The T-tail layout meant that the horizontal-tail is prone to deep-stall in certain regions due to blanketing of the flow by the wings at high angles of attack (α) as shown in Figure 19, which is adapted from NACA TMX-26 [1]. The ideal vertical region for the horizontal-tail is marked with an A. As this meant extremely large vertical-tail, as an alternative the wings were designed to have a stable pitch break such that separation occurs in the inboard part of the wing before the outboard, moving the aerodynamic centre back meaning it will generate a nose-down (negative) pitching moment. Thus wing sweep had to be reduced and there is a maximum amount of sweep not to be exceeded, given empirically as a function of taper and AR[4]. Moreover, a stick pusher or stick shaker could also be implemented to mitigate this by harshly shaking the controls if stall is imminent and hence avoid deep-stall.

As a result the vertical position was rather determined by the span of the vertical-tail (which in turn depends on the root-chord of the horizontal-tail and the volume coefficient of the vertical-tail) and was found to be $z_H = 4.01m$ from the fuselage centre-line.

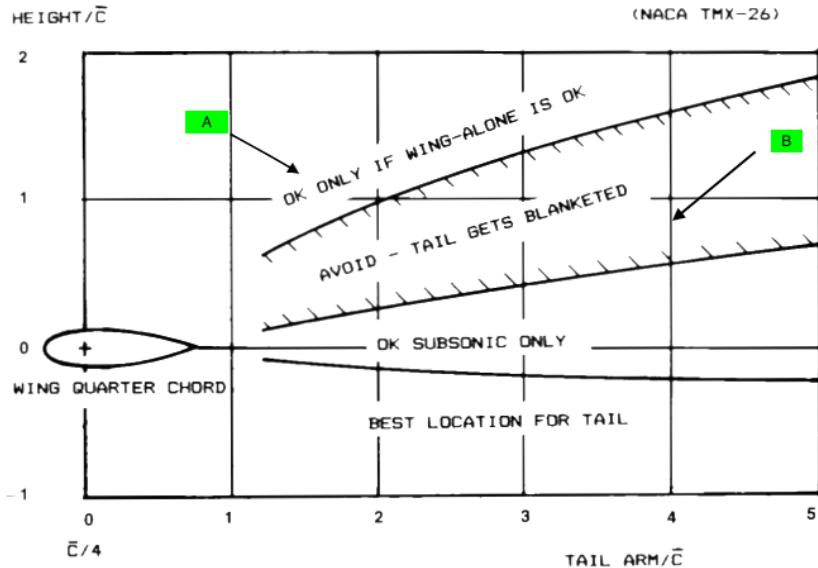


Figure 19: Effects of vertical placement of horizontal-tail on post stall behaviour.

The horizontal placement is determined by the fuselage length and vertical-tail sweep. Hence the T-tail is calculated to be $x_H = 22.5m$, which maximises the moment-arm ($x_H - x_{cg}$) and the tail-arm ($x_H - x_w$), thus increasing trimability, stability and controllability. Thus, the region selected is highlighted as B in Figure 19.

11.1.2 Area

The volume coefficient, \overline{V}_H , of a conventional horizontal-tail for jet transport is typically given as 1 [1]. For T-tail configuration, the volume coefficient is approximately 10% smaller due to the increased efficiency (higher dynamic pressure recovery and less flow disruption) hence it's taken to be $\overline{V}_H = 0.9$.

This was used as the starting point to estimate the area S_H , which is given by Equation 17. To reduce the drag and structural weight, it's desirable to have a smaller horizontal-tail, but it should still meet the trim and stability requirements, which could be achieved by increasing the tail-arm. Thus, with the above volume coefficient an initial area was calculated using the initially selected wing and horizontal-tail placements. Trim and stability was then considered and the final area was found to be:

$$S_H = \frac{\overline{V}_H S_{ref} \bar{c}}{(x_H - x_w)} = \frac{0.9(37.14)(2.3)}{(24 - 12.2)} = 6.51 m^2 \quad (17)$$

11.1.3 Aspect Ratio (AR)

The aspect ratio (AR) is an important parameter as it determines the aerodynamic efficiency of the tail and its stall characteristics. The horizontal-tail is desired to stall after the wing so that it can provide a negative pitching moment when the wing stalls. High AR reduces the stall angle of attack (α_s) but improves the lift-coefficient (C_L), thus a compromise is necessary. Furthermore, structural weight is proportional to the square-root of AR and for the T-tail layout smaller AR is clearly preferred. Since aerodynamic efficiency is not the primary objective when designing the tail-plane whereas stall characteristics, weight and structural integrity are, it was deemed necessary to minimise the AR and thus a value of 4 is chosen (typical values are in the range 3.4-6.1)[2].

11.1.4 Aerofoil Selection

The horizontal-tail aerofoil is required to have a high lift-curve slope $\frac{dC_L}{d\alpha}$ and should be operational at a wide range of α , with a high stall angle of attack (α_s). Thinner aerofoils have higher M_{crit} . Thus, it is also required that the thickness-to-chord ratio (t/c) should be 2% lower than that of the wing to ensure that the flow over the tail doesn't reach the critical mach number (M_{crit_h}) before the wing M_{crit_w} . This is to prevent the formation of shocks during a dive as that would lead to the tail-plane being ineffective and hence compromising both control or trim.

A symmetrical aerofoil is chosen as it has higher α_s when compared to a cambered aerofoil. Hence, NACA-0012 was selected due to its notable operational α in the range [-16° to 16°] as per the experimental data shown in Appendix 4 adopted from [5]. The aerofoil also has outstanding lift-curve slope of ≈ 5.73 [5]. It has t/c of 12, which is in-line with the M_{crit} requirement. Since structural weight is inversely proportional to the square-root of t/c , it implies that going for lower t/c would increase our weight, hence not desirable especially with the T-tail layout, which requires lower weight to be supported by the vertical tail (requiring less strengthening) thus leading to lower weight overall.

11.1.5 Sweep

Sweep ($\Lambda_{c/4}$) affects the tail in several ways, firstly it increases the M_{crit_H} and reduces the lift-curve slope, thus increases α_s . As a precaution it is generally taken that the horizontal-tail sweep exceeds that of the wing by 5° to increase M_{crit_H} . As extra sweep would come at the cost of weight and reduced performance, the value selected was just 5° above the wing sweep, i.e. $\Lambda_{H_{0.25c}} = 17^\circ$.

11.1.6 Taper Ratio

Since the elevator is mounted on the horizontal-tail, moderate taper values are required to provide sufficient surface. For aft-swept wings, air is pushed outwards and more lift is generated in the outboard, thus the taper-ratio is needed to reduce the tip stall tendencies introduced due to sweep. Taper is also used to provide lift distribution that's close to the elliptical lift distribution (to reduced induced drag), hence reducing tail and trim drag. Tapering would also save structural weight, reducing stresses on the vertical-tail. As a compromise of all the above, λ is selected to be 0.4 (typical values are 0.27-0.62[2]).

11.2 Vertical Tailplane

A fixed vertical-tail, with a rudder mounted on the trailing edge, is used to provide directional control, trim and stability.

11.2.1 Disposition

As discussed for the horizontal-tail, the placement it dictated by fuselage length and its sweep. Having placed it at the very back of the fuselage and with 40.44°quarter-chord sweep, the position was calculated to be $x_v = 21.14m$. The vertical position was then calculated to be $z_v = 2.74m$ from the fuselage centre-line.

11.2.2 Area

The volume coefficient, \bar{V}_v , of a conventional horizontal-tail for jet transport is typically given as 0.09 [1]. For T-tail configuration, the volume coefficient is approximately 10% smaller due to the increased efficiency (end-plate effect), thus it was taken as $\bar{V}_v = 0.081$.

Then the area S_v is given by Equation 18. The main requirement for vertical-tail sizing is the directional static stability and the case of an engine failure which results in excessive yaw. The volume-coefficient required for directional

stability is typically 0.06-0.09 [16] as discussed in the Stability Analysis section.

$$S_v = \frac{\bar{V}_v S_{ref} b}{(x_v - x_w)} = \frac{0.81(37.14)(17.24)}{(21.14 - 12.2)} = 5.80 m^2 \quad (18)$$

This value is then checked against the requirement for the engine-out scenario, which it successfully met.

11.2.3 Aspect Ratio (AR)

Vertical-tail AR is typically low to reduce the weight impact of the horizontal-tail on the vertical-tail [1]. High AR would result in larger span hence greater bending strains and aero-elastic effects could be exhibited by the tail. Moreover, low AR is advantageous as it increases the stall α of the vertical-tail to ensure it's operational during extreme cross-winds or side-slipping. Low AR also results in reduced structural weight. Thus, a value of 1 is selected (typical values lie in the range 0.7-1.2)[1].

11.2.4 Taper Ratio

For a given vertical-tail area, taper is constrained by the requirements that the vertical tip-chord (c_{t_v}) must be larger than the root-chord of the horizontal-tail (c_{r_H}) to ensure sufficient mounting surface. As a reasonable initial assumption, $c_{t_v} = 1.1 c_{r_H}$. From Section 10.1, it follows that c_{t_v} must be 2.01 m. Since AR and S_v are already selected, the root-chord c_{r_v} is given by simple geometry as:

$$c_{r_v} = \frac{2S_v}{b_v} - c_{t_v} = \frac{2(5.8)}{2.41} - (2.01) = 2.81$$

The taper-ratio is then calculated as $\lambda_v = \frac{c_{t_v}}{c_{r_v}} = \frac{2.01}{2.81} = 0.71$.

11.2.5 Aerofoil Selection

Due to the T-tail layout, the vertical-tail aerofoil t/c is crucial to ensure that the tail is strong to support the horizontal-tail whilst also reducing its own structural weight. Higher t/c gives a more stiff and stable structure and the weight is minimised. NACA-0018, which has a wide range of operational α [-20° to 20°] and a good $\frac{dC_L}{d\alpha}$ of 5.5/rads is selected. The aerofoil also has an outstanding clean $C_{L_{max}} = 1.53$. With a t/c of 18%, it would be capable of supporting the horizontal-tail. The bending and torsional stiffness are also higher due to increased thickness [2]. All the information regarding the aerofoil of choice was obtained from [26].

11.2.6 Sweep

High sweep ($\Lambda_{c/4}$) increases M_{crit_v} by effectively reducing the t/c of the vertical-tail. This reduces the likelihood of shock formation that could lead to the rudder being ineffective, thus it is required that $M_{crit_v} > M_{crit_w}$. It was also important to ensure that the drag divergence mach number M_{DD} of the vertical-tail is higher than the cruise mach number. To determine the sweep required to meet the above criteria, 2 methods were utilised i.e. the formulae given in [5] to calculate M_{DD} and check if it's higher than 0.75 and the Raymer empirical maximum mach number against sweep graph ???. The first method approximated the required $\Lambda_{c/4}$ as 36°. This is equivalent to 40° leading edge sweep using Equation 19. Thus, the critical mach number requirement was the biggest driver in sweep selection.

The high t/c chosen has led to low critical mach number of the vertical-tail (see Fig. 4.12 in [1]). To compensate for this, high sweep is required. High angles of sweep also increase the moment arm and α_s , which are highly desirable. Figure 20 shows historical trends between maximum mach number and leading edge sweep, for wings of different t/c . As a result a more conservative value of leading-edge sweep (Λ_{LE}) (since t/c of 18% is too large) of 45° is selected as it meets all the requirements stated above for maximum speed of $M=0.8$ (typical values are 33-53°[2]). The selected value also agrees with Roskam's suggested sweep vs M_{crit} for different thickness (see Figure 6.1a chapter 6 of Roskam). This is converted into $\Lambda_{c/4}$ using the geometric relationship below [1]:

$$\tan \Lambda_{c/4} = \tan \Lambda_{LE} - \frac{(1 - \lambda)}{AR(1 + \lambda)} \quad (19)$$

This gives $c/4$ sweep of 39.78°. Since this was larger than 36° required for the M_{DD} case, this value was selected.

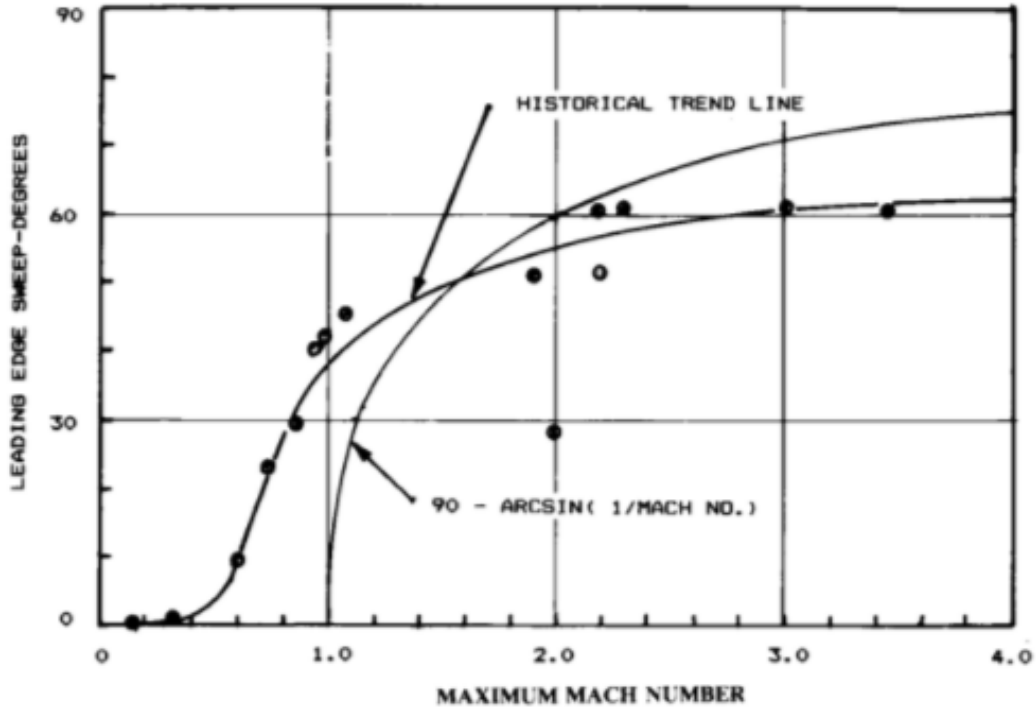


Figure 20: Leading-edge sweep angles(deg) against maximum mach number [1].

12 Aerodynamic Analysis - Tail Lift

12.1 Horizontal Tail

The zero-lift angle of attack α_{o_H} is given by the aerofoil zero-lift angle of attack (α_o) as there was no twist applied. Due to the symmetry of NACA-0012, $\alpha_{o_H} = 0$. The zero-lift pitching moment coefficient c_{m_0} is also zero since aerofoil is symmetric and the aerodynamic centre coincides with the centre of pressure.

The horizontal-tail maximum clean lift-coefficient ($C_{L_{H_{max}}}$), excluding elevator effects, is estimated using Equation 20, which takes account of the finite AR and sweep on the aerofoil maximum lift-coefficient ($C_{l_{max}}$).

$$C_{L_{H_{max}}} = 0.9C_{l_{max}} \cos \Lambda_{c/4} = 0.9(1.6)\cos(17) = 1.38 \quad (20)$$

Using $C_{l_{max}} = 1.6$ [5] (Appendix 4) and $\Lambda_{c/4} = 17^\circ$.

The horizontal-tail lift-curve slope, a_H , for a given mach number M in the subsonic and supersonic regime is estimated using the semi-empirical relation, Equation 55, which is adopted from reference [1]. This equation is highly accurate until the drag-divergence mach number [1], thus it's reasonable to use it at this stage in place of CFD analysis.

The interference between fuselage and horizontal-tail is minimal, hence the factor F is taken to be 1. T-tail configuration also means S_{exp}/S_H is 1. The aerofoil efficiency term η is taken to be 0.95[1] in the transonic regime.

Overall horizontal-tail lift coefficient (including the effects of the elevator) is then given by Equation 21.

$$C_{L_H} = a_H(\alpha_H - \alpha_{o_H}) + \frac{\partial C_{L_H}}{\partial \delta_E} \delta_E \quad (21)$$

where:

$$\alpha_H = \alpha + i_H - \epsilon = \alpha\left(1 - \frac{d\epsilon}{d\alpha}\right) - \epsilon_o + i_H$$

$$\epsilon_o = \frac{d\epsilon}{d\alpha}(i_w - \alpha_{o_w})$$

The wing down-wash effect is included as ϵ . The lift increment due to the elevator $\frac{\partial C_{L_H}}{\partial \delta_E} = a_E$ is determined empirically from [1] by Equation 22 since plain-flap form is used.

$$\frac{\partial C_{L_v}}{\partial \delta_r} = 0.9K_f \left(\frac{\partial C_l}{\partial \delta_f} \right) \frac{S_{flapped}}{S_{ref}} \cos \Lambda_{H.L.} \quad (22)$$

where:

the constant factor K_f and $\frac{\partial C_l}{\partial \delta_f}$ are determined empirically (see Appendix 5) from [1].

12.2 Vertical Tail

The vertical-tail zero-lift side-slip attack is zero, $\beta_{o_v} = 0$, since symmetrical aerofoil is used. As a consequence, the zero-lift pitching moment coefficient c_{m_0} is also zero.

The vertical-tail clean maximum lift-coefficient ($C_{L_{V_{max}}}$) is given by Equation 20. Inserting $C_{l_{max}} = 1.53$ for NACA-0018 [23] and $\Lambda_{c/4} = 39.78^\circ$ yields maximum lift-coefficient of 1.06. Again, the lift curve-slope a_v is estimated using Equation 55. Both the fuselage-spill over factor F and the ratio $\frac{S_{exp}}{S_H}$ are taken to be 1.

The overall lift-coefficient is then determined as:

$$C_{L_v} = a_v \beta + \frac{\partial C_{L_v}}{\partial \delta_r} \delta_r \quad (23)$$

where β is the side-slip angle and δ_r is the rudder deflection.

13 Control Surface Design

The tail-plane an elevator and rudder which are used for longitudinal and directional control respectively. The control mechanism chosen at this stage is a fly-by-wire (FBW) with a mechanical backup system with an artificial feel to link force to control surface position i.e. a non-reversible control system. Thus trim tabs were not deemed necessary.

13.1 Ailerons

Requirements (FAR?) roll rates?: Ailerons must be sized large enough that aircraft can be controlled laterally under several conditions within its flight envelope. Plain-flap forms are to be mounted on the trailing edge of both the left and right wing near the outer section (outboard ailerons) due to the increased moment arm. Plain-flap is chosen due simplicity and ability to deflect both up and down.

Due to the coupling between lateral and directional motion, they are risks of adverse yaw effects, hence aileron differentials were chosen, meaning the up deflection is always greater than the down deflections. Smaller down deflection leads to reduced induced drag on that wing and thus adverse yaw effects are minimised.

Inboard is mainly for high speed flights to reduce aileron reversal effects. outboard are more effective for roll control and since the aircraft operates in subsonic regime, outboard are best. Aerodynamic balancing is used.

13.1.1 Aileron Location Along Wing Span

The available span for aileron mounting is constrained by the placement of the flaps, as the span-ratio (b_f/b) is predetermined. Flaps are located near the inner section of the wing and take 70% of the semi-span ($b/2$), thus the remaining span is used for ailerons. The inner edge is hence located at 70% of semi-span($b/2$). Due to wing tip effects, ailerons must not run to the tip as the trailing vortices generated could make them ineffective. Thus, it was decided to place them 5% of the semi-span ($b/2$) away from the tip (typical value for jet transport aircraft [2]). The outer edge is hence located at 95% of semi-span($b/2$).

13.1.2 Chord-ratio (c_a/c_w) And Planform Area (S_a)

It is difficult to estimate the required aileron area as that depends on the roll-rate required, which depends on the moments of inertial of the aircraft. Thus, a historical value for similar aircraft was used to guide the required area. Nonetheless, the planform area is constrained by the available span-ratio and the aft-spar (aft-spar determines the forward position of ailerons) on the wing.

The flaps chord-ratio of 0.3 has meant that the aft-spar local chord location is given by $(c-0.3c-0.05c)=0.65c$. An extra 5% is typically added for clearance between the spar and HLDs [2]. The aft spar is also used as a mount for the hinge about which ailerons rotate, which saves weight and improve wing structural integrity.

Similar to flaps, the aileron chord-ratio is selected to be 0.3 for structural integrity, which is a typical value for similar aircrafts[2].

The ratio S_a/S_w is found to be 0.07, which agrees with typical values[2].

13.1.3 Maximum Deflections ($\delta_{a_{max}}$)

Maximum deflection of ailerons for both up and down are typically below 25° [2] to reduce risks of separation and wing stall. Moreover, near wing stall α , even slightest aileron deflection causes stall. Reduction of these deflections also decreases aero-elastic effects such as aileron reversal. To avoid wing stall, a conservative maximum deflections of $+25^\circ/-15^\circ$ (aileron differential) are chosen.

13.2 Elevator

The elevator in a plain-flap form is mounted on the horizontal-tail for pitch control and trim. Plain-flap form selected for simplicity and as it enables both up and down deflections. Requirement is that elevator must be sized large enough to control aircraft in extreme c.g. positions such as foremost c.g. position during landing and take-off. Aerodynamic balancing is used.

13.2.1 Span-ratio

Two parts (each mounted on one horizontal-tail section) are selected, the partition is due to the vertical tail running along the mid-line.

On each side, the elevator covers 95% of the semi-span (to maximise area), with 5% clearance from the root on each side. A schematic of this layout is shown below in Figure 21.

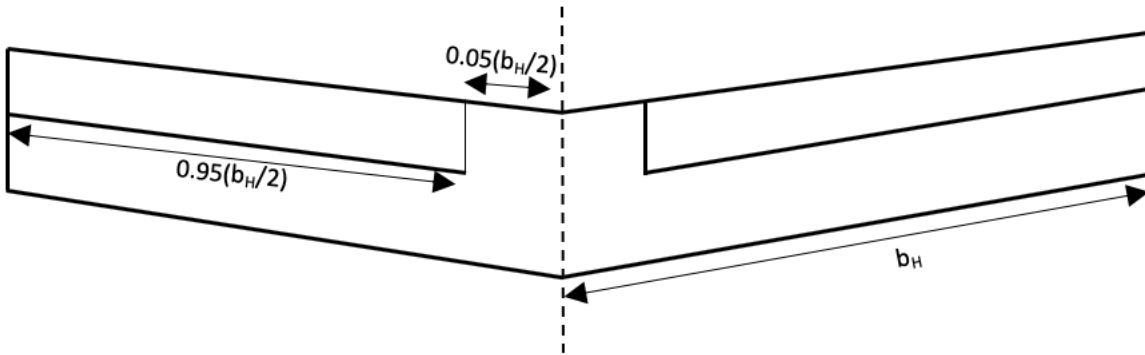


Figure 21: Elevator schematic.

13.2.2 Chord-ratio (c_e/c_H) And Planform Area (S_e)

The chord-ratio is chosen to be 0.3 to ensure sufficient elevator area. Using this, the ratio S_e/S_h is found to be 0.28 which agrees with the typical S_e/S_h for similar aircrafts [].

13.2.3 Maximum deflections ($\delta_{e_{max}}$)

Maximum deflection both up and down are taken to be $\pm 30^\circ$. This is a conservative value based on historical data [2] and it is driven by the stall requirements of the horizontal-tail.

13.3 Rudder

The rudder is key for directional control and trim of the aircraft. A plain-flap form is selected to be mounted on the trailing edge of the vertical-tail due to the increased moment-arm. Plain-flap form is selected as it is simple whilst also being effective. It also has the ability to deflect both right and left.

Aerodynamic balancing is used.

Requirements: FAR? Aircraft must be trimmable after losing an engine, which results in high yawing moments.

Placing the rudder on the vertical tail of T-tail has significant benefits as the rudder would remain unblanketed by the fuselage, wings or horizontal-tail during a spin. The entire area of the rudder is effective and thus it can be used to recover the aircraft from the spin.

13.3.1 Span-ratio (b_e/b_v)

Maximising the span-ratio is desired to increase yaw control. The span-ratio is only constrained by the clearance for down elevator deflection, to avoid the two surfaces colliding. Hence, using the maximum downward elevator deflection ($\delta_{e_{max}} = -30^\circ$) and the elevator chord-ratio (0.3) the vertical clearance needed was calculated to be 0.26m (11% vertical-tail span). As a result the span-ratio is found to be 89%, starting from the root of the vertical-tail.

13.3.2 Chord-ratio(c_r/c_v) and Planform Area (S_r)

The chord-ratio for similar aircrafts is in the range 0.25-0.4[2]. A chord-ratio of 0.3 is tentatively chosen. Using the span and chord ratios, the rudder area is approximated as a trapezoid and the ratio of areas (S_r/S_v) is found to be 0.28, which agrees with historical data for similar aircrafts [2].

13.3.3 Maximum deflections ($\delta_{r_{max}}$)

Maximum deflections of rudder is taken to be $-30^\circ/+30^\circ$. This is dependent on the aerofoil stall characteristics and it is a conservative value to avoid the vertical-tail stalling. Typical values lie in the range $\pm(15-40)^\circ$ [2].

14 Static Stability

Static stability analysis is carried out to ensure the aircraft returns to equilibrium after an external or internal perturbation.

14.1 Longitudinal Static Stability

Aircraft's' response to a perturbation in pitch is stable if $\frac{dC_m}{d\alpha} < 0$. The stick-fixed pitching moment coefficient is given by Equation 24.

$$C_m = C_{m_0w} + C_{m_0f} + \frac{dC_{mf}}{d\alpha} \alpha + \frac{x_{cg} - x_w}{\bar{c}} C_L - \eta_H \bar{V}_H C_{LH} + \frac{z_T T}{q S_w \bar{c}} \quad (24)$$

Then 2 cases of static stability i.e. power-on and power-off were considered separately.

14.1.1 Power-Off and Power-On

Differentiating Equation 24 w.r.t α and neglecting the thrust changes with α (i.e. power-off):

$$\frac{dC_m}{d\alpha} = \frac{dC_{mf}}{d\alpha} + \frac{x_{cg} - x_w}{\bar{c}} a - \eta_H \bar{V}_H a_H \left(1 - \frac{d\epsilon}{d\alpha}\right) \quad (25)$$

where:

a : overall aircraft lift curve slope (estimated using Equation 55)

$\frac{d\epsilon}{d\alpha}$: change in down-wash angle ϵ with α (empirical from [4] - see Appendix 2)

$\frac{dC_{mf}}{d\alpha}$: fuselage destabilising effects (empirical from [4] - see Appendix 2)

η_H : horizontal-tail efficiency factor (T-tails have efficiency of 1 approx. [4])

The down-wash $\frac{d\epsilon}{d\alpha}$ term is a function of the wing AR, taper-ratio, sweep, lift-curve slope ratio (compressible to incompressible flow) and the relative position of the horizontal tail from the wing [4]. Increasing AR reduces this down-wash effect i.e. increases stability and this was taken into consideration when selecting the wing AR, alongside structural weight, stall and drag.

Setting Equation 24 to zero, the neutral point (X_{np}) for all the important conditions and mach numbers is determined. In Table 4, several X_{np} values are calculated. The difference in mach number meant that the down-wash term had to be calculated for each of the conditions condition. Then the lift curve slopes at these mach numbers are calculated using Equation 55. For take-off and landing cases the effects of HLDs on the lift-curve slope of the wing was considered as discussed in HLDs design section (with $1.2\frac{c'}{c}$ extension at landing and $1.05\frac{c'}{c}$ at takeoff). Then the static margin of the aircraft in all the cases is calculated for i) when aircraft is without payload and passengers and ii) when fully loaded with payload. Typically the static margin for similar aircraft is between 4%-20% [4], hence the values calculated below agree with historical data. The biggest contributor to this stability is the horizontal-tail, which has a stabilising effect. Since the static margin requirement was fully met, the horizontal-tail volume coefficient need not be increased. It is also important to note that static margin requirement dictated the placement of components and their centre of

gravity as the aircraft $x_{c.g.}$ had to be several times adjusted to meet the 4%-20% range. For jet engines, if the engines have a destabilising effect the power-on static margin is typically 2% lower than that of power-off case.

Table 4: Static margin of aircraft

Loading condition	Flight stage	Position of x_{cg} (m)	Neutral point X_{np} (m)	Power-off static margin (% \bar{c})	Power-on static margin (% \bar{c})
MTOW (with payload)	Take-off	11.12	11.29	7.39%	5.39%
	Cruise 1	11.00	11.13	5.65%	3.65%
	Landing 1	10.99	11.37	16.52%	14.52%
	Cruise 2	10.96	11.23	11.74%	9.74%
	Loiter	10.95	11.26	13.48%	11.48%
	Landing 2	10.94	11.37	18.70%	16.70%
Without payload	Take-off	11.11	11.29	7.87%	5.87%
	Cruise 1	11.00	11.13	5.65%	3.65%
	Landing 1	10.99	11.37	16.52%	14.52%
	Cruise 2	10.96	11.23	11.74%	9.74%
	Loiter	10.94	11.26	13.05%	11.05%
	Landing 2	10.94	11.37	18.70%	16.70%

14.2 Lateral Static Stability

For lateral stability it is required that $\frac{dc_L}{d\beta} < 0$, but this is hard to quantify at this stage due to the unknown effects of the fuselage on the lifting surfaces. Thus a qualitative analysis is carried out.

The high mounted wing configuration is the most laterally stabilising factor of the aircraft, as when side-slipping by angle β the flow over the starboard wing results in increased α , thus generating a negative rolling moment. Thus aircraft is naturally stable. On top of this, the wing aft-sweep increases stability further as the rolling moment generated is negative and proportional to the sine of twice the sweep-angle $\Lambda_{c/4}$. To reduce excessive stability and increases manoeuvrability, a moderate (4°) wing anhedral is added (typical values are -5° to -3°)[1]. This reduction in lateral stability also reduced the dutch-roll frequency and increased the damping.

14.3 Directional Static Stability

For directional stability, it is required that $\frac{dc_N}{d\beta} > 0$. The fuselage typically has destabilising effects but this is determined via wind-tunnel testing. The engines are angled at 2° towards the fuselage to reduce The vertical-tail has a stabilising effects and this was taken into consideration when sizing and positioning it. The yawing moment due to the tail is given as:

$$N_v = (x_v - x_{cg})L_v \quad (26)$$

differentiating c_N w.r.t. β results in

$$\left(\frac{dc_N}{d\beta}\right)_v = \frac{(x_v - x_{cg})S_v}{S_{ref}b} a_v = \bar{V}_v a_v \quad (27)$$

To counter-act the effects of fuselage, the \bar{V}_v must at least be between 0.06 and 0.09[16]. The value of \bar{V}_v is greater than 0.09, thus aircraft is taken to be stable. Nonetheless, if aircraft is too stable directionally but not laterally, it could be unstable in spiral mode. Since aircraft is stable in both lateral and directional, this risks of unstable spiral and dutch-roll are reduced.

15 Aerodynamic Analysis - Drag Estimation

A drag analysis leading to drag polars was conducted to check the aerodynamic performance of the design. Drag is of major importance as it will ultimately depict how efficiently the aircraft operates throughout the mission profile. The major goal of this analysis was to tabulate the design glider ratio, $\frac{L}{D}$ with analytical values for each flight stage. This will dictate whether any changes have to be made to the initial sizing and set the aircraft ready for the preliminary stage. It is, therefore, expected that some design characteristics could be reviewed and amended during this analysis

in an attempt to optimise for performance.

Drag was modelled using the non-dimensional form, C_D , and was computed as a sum of its constituents forms; these being the zero-lift drag, C_{D_0} and the lift dependent drag, C_{D_l} . The zero lift drag is further sub-divided into the profile drag i.e. skin friction and pressure drag and the wave drag due to shockwave formation. This is mathematically presented in terms of non-dimensional coefficients below:

$$C_D = C_{D_0} + C_{D_l} \quad (28)$$

where:

$$C_{D_0} = C_f + C_{D_p} + C_{D_w}$$

and:

C_f : skin-friction drag

C_{D_p} : pressure drag

C_{D_w} : wave drag

C_{D_l} : lift-induced drag

Drag polars were generated for takeoff, cruise and landing considering the flight state and changes in geometry due to the retraction of high lift devices and undercarriage.

C_{D_0} was computed using the component build-up method(cite Reymer) of summing up the drag contribution of the different bodies taking into consideration the drag penalty of interference between them. Empirical data from Torenbeek and S.F Horner (cite) were also considered to fully model the design's configuration. The detailed methodology will be presented and discussed in the context of aircraft design.

15.1 Zero-Lift Drag, C_{D_0}

The zero-lift drag consists mainly of the skin-friction drag of the main component geometry. Contributions also arising from secondary features such as the up-sweep and the way the windshield is cut into the canopy of the fuselage, HLDs (high-lift devices) and undercarriage all summed up to form the miscellaneous drag, $C_{D_{misc}}$. Another term has to be added for the estimated effect of leakages and protuberances, $C_{D_{LandP}}$. The overall equation is:

$$C_{D_0} = \sum_i^n \frac{C_{f_i} FF_i Q_i S_{wet,i}}{S_{ref}} + C_{D_{misc}} + C_{D_{LandP}} \quad (29)$$

where

$S_{wet,i}$: wetted area of the component. The formulae for different parts can be found in the Appendix 9

FF_i : shape factor of component

Q_i : interference factor of component

The method used calculates the skin friction drag on a flat plate approximation for each component based on its characteristic length. The shape factor, FF_i is included to account for the geometry specific to the component and the interference factor, Q_i to account for the interference between the bodies (mainly with the fuselage).

15.1.1 Skin Friction Drag, C_f

This term is a function of Reynold's number, Re , and the characteristic length of the component as it is empirically predicted for a flat plate. Transition to turbulence and its influence to C_f had to be considered as the operational regime is transonic. It was therefore important to deduce the level of turbulent with respect to laminar flow over the different components for a more accurate estimate of C_f for operating Reynold number.BEGINNING FROM BASIC DEFINITIONS:

$$Re = \frac{\rho UL}{\mu} \quad (30)$$

where

L : characteristic length of body

μ : dynamic viscosity at altitude

Then, C_f for a laminar boundary layer:

$$C_f = \frac{1.328}{\sqrt{Re}} \quad (31)$$

And for a turbulent boundary layer:

$$C_f = \frac{0.455}{(\log Re)^2(1 + 0.144M^2)^{0.65}} \quad (32)$$

where

M : Mach number

The onset of turbulence is triggered at the critical Re . As lengthy computational techniques would be needed to calculate the critical Re for the different bodies involved it was preferred to refer on literature for the percentage of laminar and turbulent flow on similar aircraft so that a weighted average of the skin friction coefficient could be calculated using both equations as follows:(cite Reymer).

$$C_f = k_{laminar} C_{flaminar} + (1 - k_{laminar}) C_{fturbulent} \quad (33)$$

where

k : the percentage of laminar flow

Considering the aircraft is operating at a $Re = 8e06$ it and that $Re_{crit} = 10e05$ for a flat plate it is highly unlikely that any laminar flow will occur. It is not expected that any adverse pressure gradients will be large enough to return the flow to laminar therefore $k_{laminar} = 0$.

15.1.2 FF_i And Q_i

The form factor corrects for a body's camber and thickness characteristics. The form factors for the main aircraft components based are as follows[1]:

$$FF_{fuselage} = 1 + \frac{60}{f^3} + \frac{f}{400} \quad (34)$$

$$FF_{wing} = \left[1 + \frac{0.6}{(x/c)_m} \left(\frac{t}{c} \right) + 100 \left(\frac{t}{c} \right)^4 \right] [1.34M^{0.18} (\cos \Lambda_m)^{0.28}] \quad (35)$$

$$FF_{tail} = 1.1 \left[1 + \frac{0.6}{(x/c)_{m,h}} \left(\frac{t}{c} \right)_h + 100 \left(\frac{t}{c} \right)_h^4 \right] [1.34M^{0.18} (\cos \Lambda_{m,h})^{0.28}] \quad (36)$$

$$FF_{nacelle} = 1 + \frac{0.35}{f} \quad (37)$$

where

$(x/c)_m$:chord-wise location of the maximum thickness

$(\frac{t}{c})$:thickness to chord ratio

Λ_m :Sweep of the maximum-thickness line

Notes:

- The subscript h is used for tail values
- The 10 % rise in the form factor for the tailplane is due the hinge of the control surface

The interference of the fuselage is negligible (i.e $Q = 1$) as it is much larger relative to other bodies. The interference originating from the corners of the wing-fuselage configuration is negligible because of a high wing configuration and well blended and filleted wing root[1]. The interference of the engine nacelle is also negligible as it is placed more than two diameters from the fuselage. Q is therefore assumed 1 for both nacelle and wing for this section. For the tail, interference between the junctions with the fuselage and the corners formed between vertical and horizontal tailplanes could not be neglected. Looking at empirical data of various configurations in Hoerner [34], interference was deduced to amount for a 4% increase on top of the clean drag for a conventional t-tail thus $Q = 1.04$.

15.1.3 $C_{D_{misc}}$

The miscellaneous drag terms come mainly from empirical data and equations. Fuselage contributions to $C_{D_{misc}}$ arise from the upsweep of the rear and the pods for the undercarriage. The upsweep drag contribution was modeled by considering the upsweep angle as shown:

$$C_{D_{upsweep}} = 3.83 \frac{A_{max}}{S_{ref}} \beta^{2.5} \quad (38)$$

where

A_{max} : the maximum cross-sectional area of the fuselage

The pods were approximated to contribute to an additional drag of 0.2 based on frontal area. For takeoff and landing HLD and undercarriage drag has to be also considered. This was found by summing up all the contributions of the parts that make the undercarriage and the gear wells. These were found in literature as non-dimensional "drag areas", D/q per unit area (i.e drag coefficients based on frontal area). An area swap was needed again.

$$6 \times \Delta \frac{D/q}{A_{frontal}} = 0.25 \text{ - Wheels and tyre}$$

$$3 \times \Delta \frac{D/q}{A_{frontal}} \text{ - Round struts}$$

$$\implies 1.2 \sum \Delta \frac{D/q}{A_{frontal}} =$$

Note that a 1.2 factor accounts for the mutual interference of the wheels.

Then the overall undercarriage drag:

$$C_{D_{u/c}} = 1.07 \times \frac{D/q}{A_{frontal}} \frac{S_{frontal}}{S_{ref}} = \quad (39)$$

Note that a 7 % increase is due to the gear wells left open.

For the extended flaps the drag rise is:

$$C_{D_{HLD}} = 0.0023 \frac{b_f}{b} \delta_f \quad (40)$$

where

b_f :relative span of flaps

b :wing span

The final considerations is the drag of the pylon, $C_{D_{pylon,frontal}} = 0.1$, and a 4 % increase to the overall C_{D_0} due to leakages and protuberances. Table .. shows all of the contributions and the total $C_{D_{misc}}$.

15.1.4 Wave Drag And Sweep

Wave drag is defined as the drag rise associated with energy losses due to shockwaves. Wave drag occurs above M_{crit} therefore has to be considered only during the first cruise for which it was decided that $M_{cruise} = M_{DD}$, exploiting both the performance benefits of a high mach number while preventing large wave drag penalties that occur beyond this. The drag rise at M_{DD} is by definition 0.002. As M_{cruise} was a predetermined value the wing was forced to have an equal value for M_{DD} by optimising the sweep angle. The procedure involved the use of empirical data from Raymer(cite). For the wing:

$$M_{DD} = (M_{DD})_{L=0} LF_{DD} - 0.05 C_{L_{design}} \quad (41)$$

where

$(M_{DD})_{L=0}$: M_{DD} at zero lift

LF_{DD} : lift adjustment factor

LF_{DD} is a function of C_L at cruise and $\frac{t}{c}$. The shock delaying characteristics of supercritical aerofoils was considered by multiplying the $\frac{t}{c}$ by a factor of 0.6. LF_{DD} was graphically found using Figure 22.

Re-arranging Equation 41 for $(M_{DD})_{L=0}$:

$$(M_{DD})_{L=0} = \frac{0.75 + 0.05 \times 0.4}{0.96} = 0.8021 \quad (42)$$

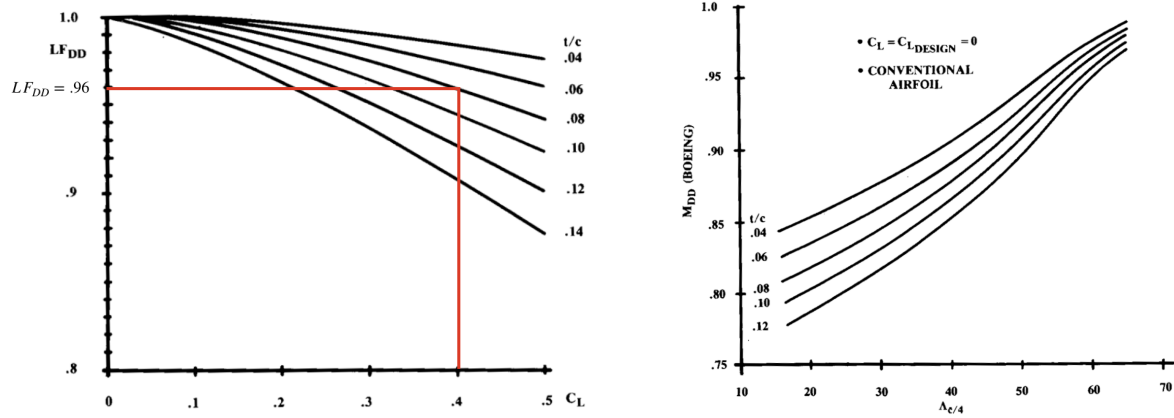


Figure 22: Lift adjustment for M_{DD} (left) using a 'conventional transformation' of $\frac{t}{c} = 0.0840$. LF_{DD} is 0.96. $(M_{DD})_{L=0}$ against sweep angle (right) [1].

The sweep angle was found graphically to be 12 deg via extrapolation using Figure 22. For the fuselage, M_{DD} is a function of dimensions dimensions alone. It was found graphically using the subsonic curve in Figure 23 to be $M_{DD} = .78$. Being larger than the wing's it is expected that shockwaves begin to appear earlier on the wing and thus the wave drag can be assumed to originate only from the wing.

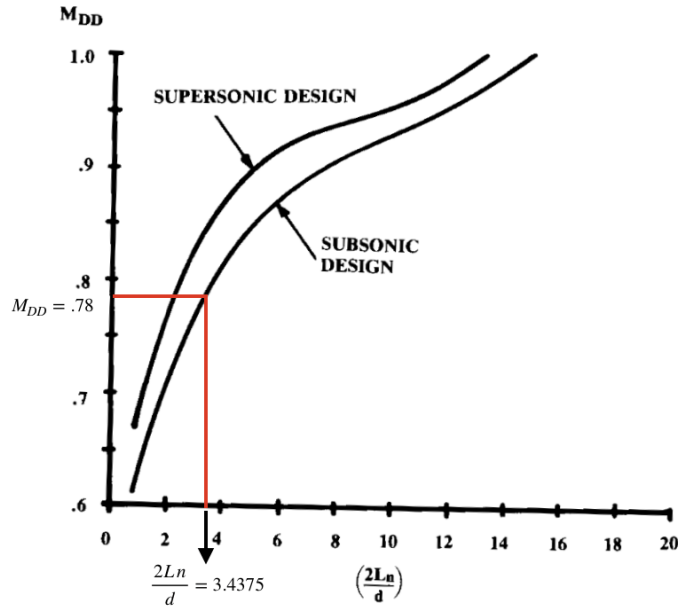


Figure 23: (M_{DD}) of fuselage based on distance from nose to constant diameter and effective diameter [1].

The complex nature of the wave drag rise can be approximated as a function of the the critical Mach number in the form:

$$\Delta C_{D_w} = a \left(\frac{M}{M_{crit}} - 1 \right)^b \quad (43)$$

where

$a=0.1498, b=1.6884$ are aircraft specific parameters that can were adopted and adjusted from similar types of aircraft(cite Roskam 2).

Although operating at M_{dd} , the drag rise is provided below to model how the wave drag behaves with Mach number.

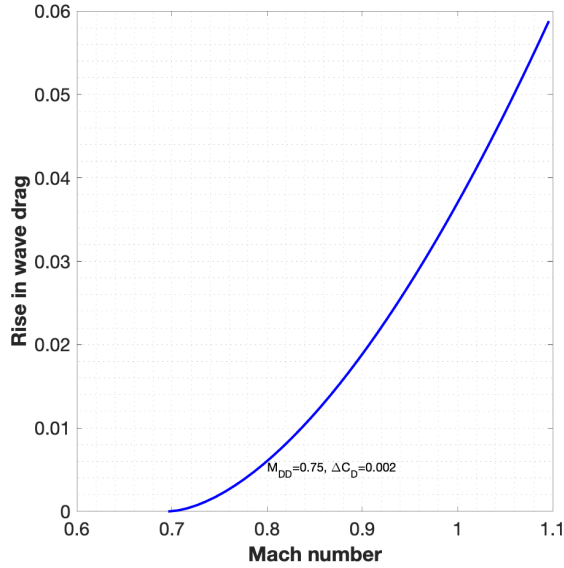


Figure 24: Rise of wave drag with Mach number

15.1.5 Overall Drag, C_D

For the total drag the lift induced drag components must be included for the trimmed aircraft:

$$C_D = C_{D_0} + K_w [C_{L_a}(\alpha + i_w - \alpha_{ow})^2 + \eta_H \left(\frac{S_h}{S_{ref}} \right) K_h C_{L_h}^2] \quad (44)$$

where

$$K_w = \frac{1}{\pi A R_w e_w}$$

$$K_h = \frac{1}{\pi A R_h e_h}$$

For landing and takeoff the additional induced drag due to flaps is:

$$\Delta C_{D_i} = k_f^2 \delta C_L^2 \cos \Lambda_c / 4 \quad (45)$$

where

$k_f = 0.28$, partially flapped wing

The Oswald efficiencies of wing and tail were estimated according to Howe 2000 (cite him - add reference) for subsonic and transonic flows:

$$e = \frac{1}{[1 + 0.12M^6] \left[1 + \frac{0.142 + f(\lambda)A[10(t/c)]^{0.33}}{(\cos \Lambda_c/4)^2} + \frac{0.1(3N_e + 1)}{(4 + AR)^{0.8}} \right]} \quad (46)$$

where

N_e : number of engines on wing

$$f(\lambda) = 0.005(1 + 1.5(\lambda - 0.6)^2)$$

The drag polars were finally generated for the conditions of takeoff, cruise 1, cruise 2, loiter and landing as show in Figures NUMBERS. This was done by varying the α_{inf} , hence C_L to get the variation of drag. The operational C_L were then used where applicable to deduce the glider ratios, $\frac{L}{D}$ to be later used in the performance evaluation of the aircraft. Drag was higher in take-off and landing configurations relative to cruise and loiter by almost an order of 10 as expected. However, the values were overall excessively larger than the values estimated during the Baseline configuration which consequently led to much lower $\frac{L}{D}$ values. After looking at the breakdown of the drag components it was concluded that the C_{D_0} was for all flight stages higher than expected due to the skin friction contributions of the fuselage and wing.

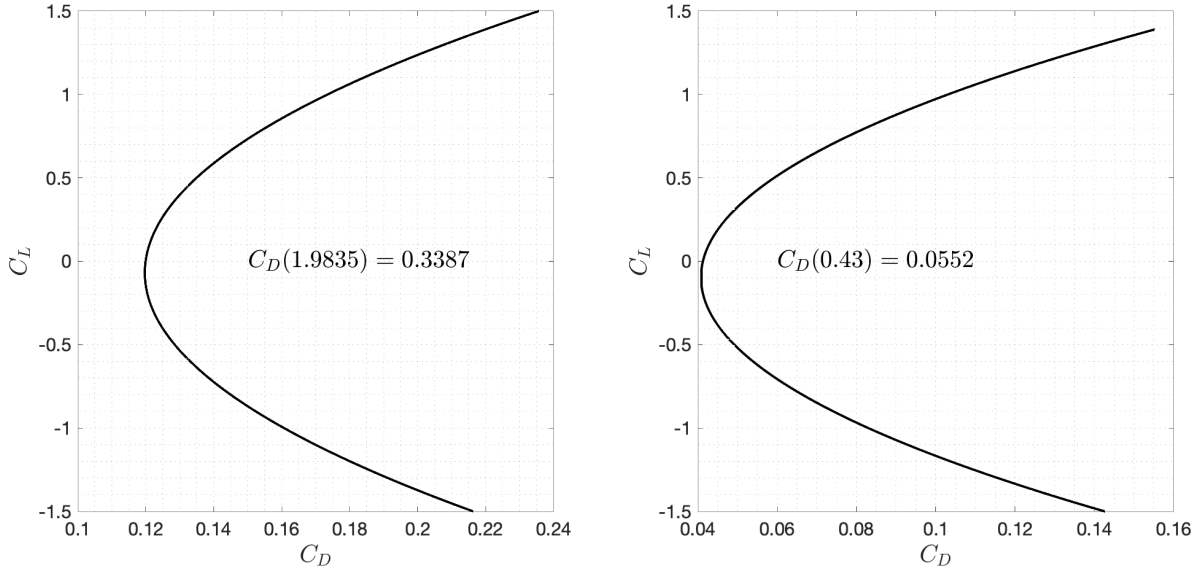


Figure 25: Drag polars for take-off (left) and Cruise 1 (right). $L_{D_{cruise1}} = 7.7899$; The operating C_D is given as a function of the respective C_L

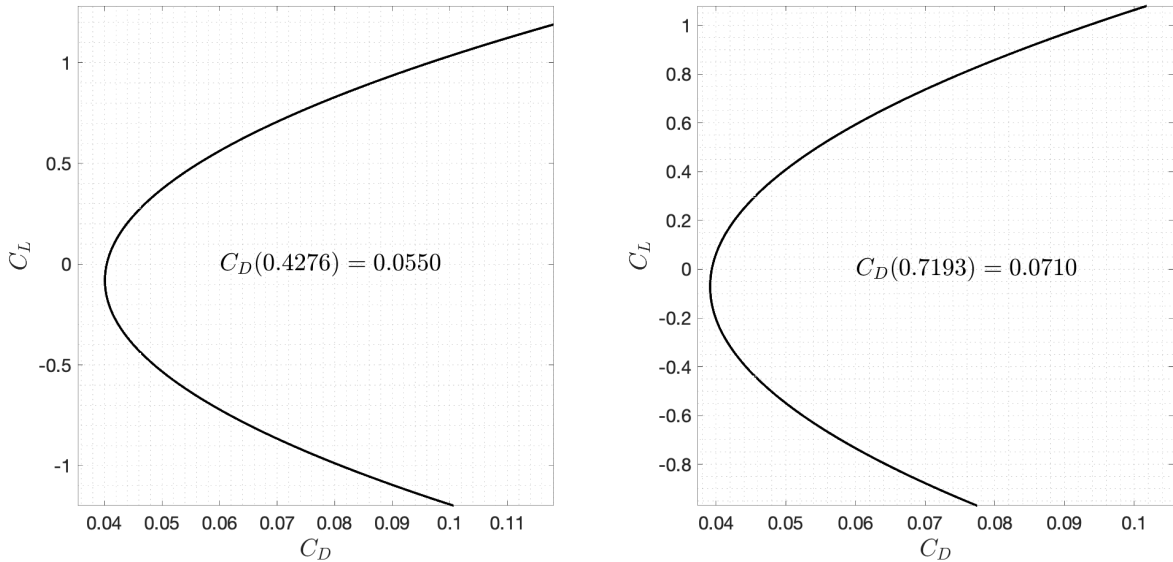


Figure 26: Drag polars for Cruise 2 (left) and Loiter (right); $L_{D_{loiter}} = 10.1310, L_{D_{cruise2}} = 7.7745$. The operating C_D is given as a function of the respective C_L

16 Trim Analysis

To meet the requirement that the aircraft should be trimmable at different flight conditions within its flight envelope, a fixed horizontal-tail with an elevator is selected. The horizontal-tail setting angle i_H is then calculated for the design lift coefficient i.e. the cruise lift-coefficient. This is so as to minimise trim drag during the dominant segment of the flight i.e. cruise. Trim drag is the lift induced drag produced as a result of the increased horizontal-tail lift which changes the total lift generated and thus increases induced drag both on the wing and tail-plane. Hence, producing as minimum lift in the tail to trim the aircraft is key.

Depending on the contribution of the wing in pitch (whether wing is located before or aft of the centre of gravity), i_H could either be positive or negative. After calculating the aircraft x_{cg} at the cruise, the required i_H to keep the aircraft in trim i.e. $c_m = 0$ is found with the elevator deflections at zero.

Thus Equation 24 was set to zero and then the required C_{L_H} was calculated by re-arranging the equation and setting

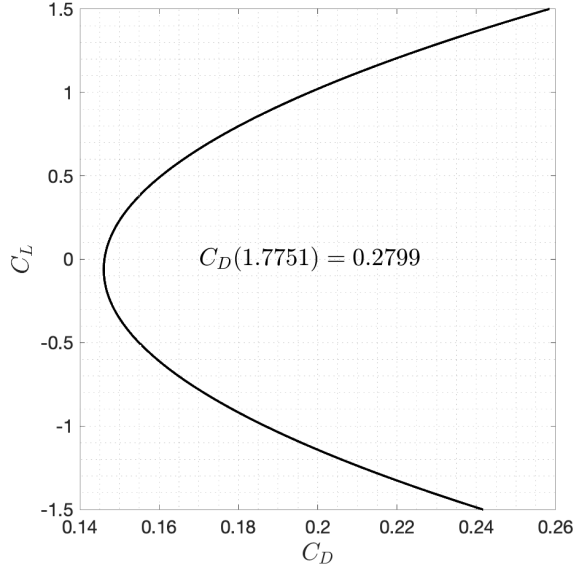


Figure 27: Drag polar for Landing. The operating C_D is given as a function of the respective C_L

C_L to be equal to the cruise lift-coefficient estimated by Equation 47.

$$C_{L_{cruise}} = \frac{W_{cruise}}{0.5\rho S_{ref} V^2} = 0.43 \quad (47)$$

where the cruise weight is estimated during the initial weight sizing stage. Note that the thrust was assumed to be equal to drag. The cruise drag was estimated from the L/D value of the cruise selected in the initial sizing stage i.e. $0.866(\frac{L}{D})_{max}$.

The required C_{L_H} for trim was -0.47. Then using Equation 21 and re-arranging to give:

$$i_H = \frac{C_{L_H}}{\eta_H a_H} + \alpha_{oH} + \epsilon_o - (1 - \frac{d\epsilon}{d\alpha})\alpha \quad (48)$$

since horizontal-tail is symmetric, $\alpha_{oH} = 0$. From static stability analysis, $\eta_H = 1$.

Replacing α with $(C_L - C_{L_o})/a$, where C_{L_o} is the lift-coefficient at zero angle of attack, yields:

$$C_{L_o} = a_w(i_w - \alpha_{ow}) + \eta_H a_H \frac{S_H}{S_{ref}} (i_H - \epsilon_o) \quad (49)$$

This was then solved to find that $i_H = -2.07^\circ$. This falls in line with the typical values of between -3° to 15° [5]. To determine the trim capability of the aircraft and the required elevator deflection to trim the aircraft at each of the conditions. Hence, for a given elevator deflection within the range $[-25^\circ$ to 25°], the pitching moment was plotted against the lift-coefficient (as a sum of the wing and horizontal) for a range of angles of attack was plotted. The effects of the horizontal-tail and elevator deflection are taken into account. Moreover, the down-wash term $\frac{d\eta}{d\alpha}$ for the given mach number was calculated. Since the trim capability is dependent on the position of the c.g., the x direction c.g. position were taken from Table 4. Then at the required lift-coefficient, the elevator deflection that results in zero pitching moment is selected. The plots for the several conditions can be found in Appendix 7. Note that the effects of HLDs due to their respective deflection on the lift-curve slope of the wing is taken into account when calculating the pitching moment. The elevator is a plain flap and thus doesn't change the lift curve slope of the horizontal-tail.

The wing zero-lift pitching moment $c_{m_{ow}}$ is empirically determined (see Appendix 3). The fuselage pitching moment at zero angle of attack i.e. $C_{m_{of}}$ could be accurately approximated using CFD analysis as it is dependent on the up-sweep angle of the fuselage. The overall pitching contribution of the fuselage is given by:

$$c_{m_f} = \frac{dc_{m_f}}{d\alpha} (\alpha - \alpha_{of}) \quad (50)$$

typically α_{of} is $1\text{-}2^\circ$ and assuming a value of 2° , $C_{m_{of}}$ was found to be -0.09.

The thrust term is calculated by thrust matching and hence the drag force equals to the thrust. The drag values used are the actual drag calculated in the Drag Estimation section.

Table 5: Trim considerations for different loading and operational conditions

Loading condition	Flight stage	Position of c.g.(m)	Elevator deflection δ_E (degree)
MTOW (with payload)	Take-off	11.12	-14.65
	Landing 1	10.99	-17.00
	Landing 2	10.94	-18.05
Without payload	Takeoff	11.11	-14.68
	Landing 1	10.99	-17.00
	Landing 2	10.94	-18.05

17 Performance Estimation

It had to be made sure that the aircraft could take-off and land and have a balanced field length all within the limits of FAR25. What is more it had to be validated that the aircraft can indeed achieve the cruise range and also its endurance deduced. Being the driving factor of range, the low values of glider ratios evaluated during the drag analysis have had a deteriorating effect on performance. For the calculations below, V_{stall} was computed for takeoff and landing separately based on the weights, operational Mach Number and flap deflection. In an attempt to capture the overall performance a specific excess power envelope is provided at the end of this section.

17.1 Takeoff Distance

The calculated takeoff distance 958.8m was lower than the actual takeoff distance 1300m estimated from the baseline configuration. To calculate the takeoff distance the formulas from (REFERENCE HERE) were used with the following aspects considered: 1) L_D was taken from the drag polar for the C_{Lclimb} , i.e. $C_{Lmax}/1.2^2$ as per FAR 25 2) The maximum thrust to weight ratio was considered, i.e. $T/W_0 = 0.36$ 3) Since the lift at touch down was not equal to the weight the lift coefficient touch down was found using the lift curve slope for the wing setting angle, i.e. $\alpha = i_w$. 4) The contribution of the horizontal tail-plane was neglected 5) The obstacle height was found to be lower than the transition height, implying that no extra climb distance had to be added and the appropriate transition distance had to be considered.

17.2 Balanced Field Length

The bypass ratio was taken from the engine manual as 6.2 to 1. For the calculations of the climb gradient, γ_{C_L} , the dimensional drag of one engine inoperative had to be considered. This was done using $C_{D_{in}}$ and adding the effect of the windmilling of the inoperative engine, which is 0.3 based on frontal area. This effect was converted into a contribution as previously mentioned. A dimensional analysis was carried out as the formula includes empirical constants in feet, and everything was converted to feet at the end. From the equation (reference) the balanced field length was found to be 359 m.

17.3 Landing

the landing distance was evaluated with the same concepts as the takeoff height by working in reverse. The following things were considered: 1) $V_{touchdown} = 1.15 * V_{sland}, V_{flare} = 1.23 * V_{sland}$. 2) The landing C_L was taken as the one at $V_{approach}$ i.e $C_{Lmax}/1.3^2$ 3) Thrust reversers were considered to be running until the cutoff speed of 25.72 m/s and then switched-off (idling engine) to prevent the engine being damaged from suction of exhaust gases. The landing distance was found to be 717 m which lies within FAR 25 restrictions and was lower from the one estimated in baseline configuration.

17.4 Range, Endurance and Specific excess power

In order to evaluate the range of the aircraft, it was important to re-estimate the weight fractions of loiter and Cruise 2 based on the real values of glider ratios and specific fuel consumption. This was done using the Breguet Range Equation in its original form (REFERENCE).The range of the aircraft was evaluated to be only 565 km, much lower than the required mission profile range. This was the consequence of the low glider ratios. This means that the aircraft fails to accomplish the mission profile. A re-design of the fuselage dimensions leading to a lower cross-sectional area would lead to higher glider ratios and increased performance. The specific excess power envelope in Figure shows the aircraft can achieve the maximum ceiling of 42000 ft required as shown at contour 0. The aircraft will operate within the envelope during cruise as marked by the asterisk and can accelerate or climb accordingly within the performance based on excess power.

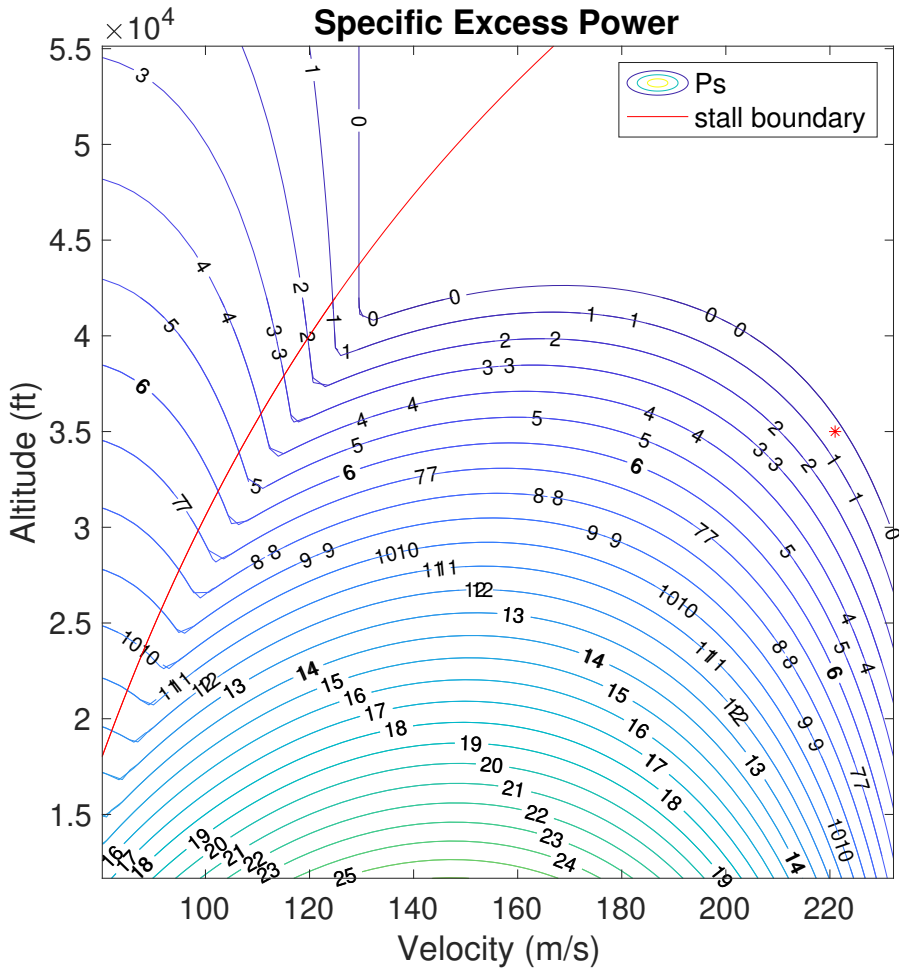


Figure 28: Specific Excess Power envelope with contours of constant velocity in altitude against velocity. The operational regime in cruise is marked with a red asterisk.

18 Discussion Of Overall Design

The aircraft design was filled with compromises between several considerations such as structural integrity, aerodynamic performance, structural weight minimisation and safety and regulatory requirements.

Firstly, the diameter of the aircraft was driven by the compromises for drag, landing gear positioning, the cabin layout and the centre of gravity location. The performance of the aircraft, especially the cruise drag, was significantly affected by the chosen diameter. Initially, the outer diameter of the fuselage selected was 2.6m. In this layout, the cargo compartment was smaller than 0.6m (i.e. the minimum FAR 25 height requirement) which meant that the cargo had to be placed somewhere else on the aircraft. The only feasible option was to place the luggage at the back near the tail. Considering the centre of gravity position, it was found that the x-direction c.g. was near the up-sweep point (i.e. the change in constant diameter of the fuselage). This would mean that the main undercarriage is very close to the up-sweep point because they needed to take about 80% of the overall weight. We thought that placing the main landing gear at such a position isn't preferred as there would be no sufficient volume for their retraction and attachment. Moreover, since the floor of the cabin could not be placed at the very bottom of the fuselage, there was a 0.5m gap in the underbelly. This volume was not utilised efficiently, with only a few systems occupying less than 90% of the available volume.

To mitigate for the above problems, it was deemed necessary for the diameter to be increased to facilitate for the compliance with FAR 25 for the underbelly cargo requirement, thus eliminating the need to place the cargo at the tail and also the main landing gear would be placed forward.

In hindsight, we could have kept the diameter at 2.6m and moved the wing forwards to compensate for the shift in the CG due to the cargo being placed at the back. This would have also increased our moment arm, reducing the size of the vertical and horizontal tails. This would also mean reduced overall induced and trim drag. The smaller of the fuselage would have also meant lower zero-lift drag due to the reduced frontal area. This all combined would have

improved our lift-to-drag drag ratio for cruise and thus yielded a higher achievable range for the second cruise. The lack of experimental data for several aerofoils has narrowed our choice when selecting the optimum wing to minimise drag at cruise. The data extracted from xfoil isn't experimental, and thus we could not rely on it when determining the maximum lift-coefficient and stall angle of attack. For our selected aerofoil, this meant that we had to look at similar supercritical aerofoils to validate the lift-curve slope as there was no experimental data to cross-check against.

The requirement for large additional C_L at landing and takeoff has led to much larger flaps been needed than previously predicted during the initial sizing stage. The only feasible solution was to select a more complex HLDs that could provide the necessary change in C_L . This complexity would mean that the structural weight of the actuators and the supporting mechanism will be increased.

Since the lift change is dependent on the flapped area of the flaps, they were selected to occupy approximately 75% of the semi-span on each side thus, the aileron size decreased. The extension of the flaps also affects the lift, and hence 30% of the chord was occupied by the flaps. This meant that during deflection, the interaction of the flaps with the exhaust of the engine was inevitable. Hence the vertical height of the pylons had to be increased. This could have been avoided had we split the HLDs in the exhaust wake region, but this would have meant smaller flapped area and hence wouldn't have met required C_L at landing.

The biggest challenge of the baseline configuration was the high-mounted wing that dictated the design criteria of other parts. One of the main difference compared to a low mounted-wing design was the location of the main undercarriage, as for our aircraft it had to be placed in the fuselage instead of the wings. This increased our fuselage diameter as the main gear did not fit in a typical 3.0m diameter. This affected our drag performance as the drag is proportional to the diameter of the fuselage. On the other hand, a bigger diameter allowed the cargo to be placed in the underbelly as staff can work in the hold without having to crawl with an underbelly height of 0.90m. Not having the cargo in the tail like most of other 50 passenger aircraft, simplified calculations for the centre of gravity location as a big contribution of the total weight is not anymore in the back of the aircraft but can be placed with more freedom in the underbelly at our desired x-location. Not having the cargo in the tail resulted in the centre of gravity closer to the nose and more importantly to the payload location, meaning small differences were found between the centre of gravity location for configurations with and without a passenger. Finally, having a larger diameter highly increases the comfort of the passenger and gives more freedom to cabin designers. Therefore, comparing our model to similar-sized aircrafts with low mounted wings, we obtained a more flexible centre of gravity location, better clearance for the engines and a more comfortable cabin layout at the expense of an increase in fuselage drag.

The engine CF-34 did not give the closest thrust to the thrust value our aircraft required. This was made due to the lack of information associated with the Honeywell HTF7000 engine that would have been a better fit. Indeed choosing an engine which thrust settings are further from the required ones led to higher inaccuracy.

The undercarriage as expected led to higher drag penalty that could be avoided had we used a more complex retraction mechanism. The primitive straight folding struts had to come with a pod in pair which inevitably increased the wetted area of the fuselage and hence increased the drag. Using a more complex angled strut with multiple hinges and rotational points would have indeed been advantageous (e.g. BAE 146). However, the 'imagination field', when dealing with such complex oleos in this project, would have had no boundaries, and the justification for certain design criteria would be vague. Obviously, a complexity of BAE undercarriage comes at a price, but the price was unknown and incalculable. On the other hand, trivial straight struts provided a solid compromise between the overturn angle and the gear retraction, and gave a deep insight of gear dimensional analysis.

High wings meant undercarriage cannot be mounted on wings and thus span loading was not taken advantage of. The post-stall behaviour (discussed in horizontal-tail design) added another complexity to the vertical-tail design as the height constraint (as a function of the tail-arm) contradicted with the volume coefficient initially selected. A small vertical-tail would not meet the height requirement while satisfying the taper-ratio and the requirement that the tip-chord must be at least 10% than that of the horizontal-tail root-chord to provide sufficient mounting surface. To resolve this issue, either the wing had to move back, i.e. increasing tail area or keeping the wing position fixed but increasing the horizontal-tail area (extra-area beyond what's needed). Moving the further wing-back would be detrimental as it reduced the static margin and thus increasing the vertical-tail area would lead to higher drag. Thus, the wings were designed to have a stable pitch break.

References

- [1] Raymer, Daniel P. *Aircraft Design : A Conceptual Approach*. Sixth ed. 2018. Print. AIAA Education Ser. pages 1, 4, 6, 7, 8, 17, 18, 21, 22, 23, 24, 25, 28, 30, 32, 45
- [2] Roskam, Jan. *Airplane Design. Part 1, Preliminary Sizing of Airplanes* Ottawa: Roskam Aviation and Engineering Corporation, 1985. Print. pages 7, 8, 22, 23, 25, 26, 27, 43
- [3] Torenbeek, Egbert. *Synthesis of Subsonic Airplane Design : An Introduction to the Preliminary Design of Subsonic General Aviation and Transport Aircraft, with Emphasis on Layout, Aerodynamic Design, Propulsion, and Performance*. 1982. Print. pages 1, 3, 4, 7, 42, 47
- [4] Lecture Notes. Imperial College London, Department of Aeronautics, South Kensington Campus, SW7 2AZ, UK, 2019/2020. AVD lecture notes. pages 21, 27, 44
- [5] 1. Abbott I, Doenhoff A. New York: Dover; 1949. *Theory of wing sections, including a summary of aerofoil data*. pages 22, 23, 24, 35, 44
- [6] Charles D. Harris. Langley Research Center, Hampton: Virginia; 1960. *NASA Supercritical aerofoils: A Matrix of Family-Related aerofoils*. pages 4
- [7] Güzelbey İ, Eraslan Y, Doğru M. 2019. *Effects of Taper Ratio on Aircraft Wing Aerodynamic Parameters: A Comparative Study*. European Mechanical Science. pages 7
- [8] Selig M, Guglielmo J, Broeren A, Giguere P. 1997. *Summary of low-speed aerofoil data*. Virginia Beach, Va: SoarTech Publications. pages 4
- [9] Unknown Author. Asphalt Pavement Alliance. <http://www.asphaltroads.org/why-asphalt/why-choose-asphalt/> pages 17
- [10] Airport Information. <https://www.airnav.com/airport/> pages 17
- [11] Data Section-Tires. <https://www.goodyearaviation.com/resources/pdf/tire-specifications-6-2018.pdf> pages 17
- [12] Good Year Aviation. Akron, Ohio; 2002. *Aircraft Tire Data Book. Data Section-Tires*. pages 18
- [13] Dr Qianqian Li. Imperial College London; 2018. AE2-208. Materials. 2 Alloys. Ti alloys. pages 18
- [14] Chris Grosenick. 2003. *Accumulators: Hydraulic energy storage*. <https://www.aviationpros.com/home/article/10387187/accumulators-hydraulic-energy-storage/>. pages 10
- [15] Parker Aerospace. Kalamazoo, Michigan; 2009. *Engine Driven Pumps. Product Specification Sheet*. pages 10
- [16] Levis E. Imperial College London, 2018. AE2-211: *Mechanics of Flight lecture notes (Chapters 1 & 2 and 9-12)* pages 6, 23, 28
- [17] Antonio Carozza. April 26 2017. *Heat Exchangers in the Aviation Engineering*. pages
- [18] Isodoro Martinez. 1997-2019. *Aircraft Environmental Control*. pages 10
- [19] Jack D. Mattingly. 1987. *Aircraft Engine Design*. pages 14
- [20] Lowry JG, Polhamus EC. *A method for predicting lift increments due to flap deflection at low angles of attack in incompressible flow*, National Advisory Committee for Aeronautics, Technical Note No. 3911, 1957. pages
- [21] Springer Science+Business Media, LLC 2012. *Airbreathing Propulsion: An Introduction*. pages 14, 15
- [22] Alison B. Evans, NASA, 1991. *The Effects of Compressor Seventh-Stage Bleed Air Extraction on Performance of the F100-PW-200 Afterburning Turbofan Engine*. pages
- [23] Harry J Goett, W. Kenneth Bullivant. *Tests of N.A.C.A 0009, 0012 and 0018 aerofoils in the full scale tunnel*. pages 11, 25
- [24] V. Madonna, P. Giangrande, and M. Galea. *Electrical Power Generation in Aircraft: review, challenges and opportunities*. pages 11
- [25] Cranfield University. Meng Fanliang. 2011. *Actuation System Design With Electrically Powered Actuators* pages 12

- [26] Eastman N. Jacobs and Ira H. Abbott. Report No. 669. *Airfoil section data obtained in the N.A.C.A. variable-density tunnel as affected by support interference and other corrections.* pages 23
- [27] Airworthiness Standards FAA FAR part 25 pages 1, 20
- [28] Ajoy Kumar Kundu. 12 April 2010. *:Aircraft Design. Cambridge University Press.* pages 1
- [29] Gary A. Crowell Sr. 1996 *The Descriptive Geometry Of Nose Cones* pages 3
- [30] Roskam, Jan. *Airplane Design. Part 2, Preliminary Configuration Design and Integration of the Propulsion System: Roskam Aviation and Engineering Corporation, 1985. Print.* pages 3
- [31] Levis E. Imperial College London, 2019. *Weight Balance Estimation for Transport Aircraft* pages 12, 13
- [32] J.A. Yetter NASA 1996. *Why Do Airlines Want And Use Thrust Reversers* pages 16
- [33] January 1999 *Aerofoil maximum lift coefficient for Mach numbers up to 0.4. ESDU 84026* pages 5
- [34] January 1965 *Hoerner SF. Fluid-Dynamic Drag, published by the author. Midland Park, NJ. 1965:3-19.* pages 30

19 Appendix

19.1 Appendix 1

19.1.1 Prandtl-Glauert correction

$$C_p = \frac{C_{p_i}}{\sqrt{1 - M_\infty^2}} \quad (51)$$

Using the Bernoulli's equation for compressible flow at $M=1$

$$C_{p_{crit}} = \frac{2}{\gamma M_\infty^2} \left[\frac{2 + (\gamma - 1)M_\infty^2}{\gamma + 1} \right]^{\frac{\gamma}{\gamma-1}} - 1$$

(52)

The value of M_{crit} was found by setting the value of $C_{p_{crit}}$ equal to C_p in Equation 48 and solving for M_{crit} .

19.1.2 Aspect ratio variation

The range of AR variation was found to be lying within the conditions (1) and (2). Condition (1) lies on the empirical formula that relates the optimum C_L at cruise with the aspect ratio by considering the maximum Lift to Drag ratio [3]. Condition (2) also relates the C_L at cruise optimal conditions by taking into account the minimum Drag.

$$(1) Cl_{opt} = 0.17 \cdot \sqrt{AR} \rightarrow AR_1 = 6.4546$$

$$(2) Cl_{minD} = \sqrt{Cd_0 \cdot \pi \cdot AR} \rightarrow AR_2 = 9.89612$$

19.1.3 Sweep angle at the leading edge equation

$$\Lambda_{LE} = \tan^{-1} \left[\tan \Lambda_{c/4} + \frac{1 - \lambda}{AR \cdot (\lambda + 1)} \right] \quad (53)$$

19.1.4 Twist angle ϵ_t

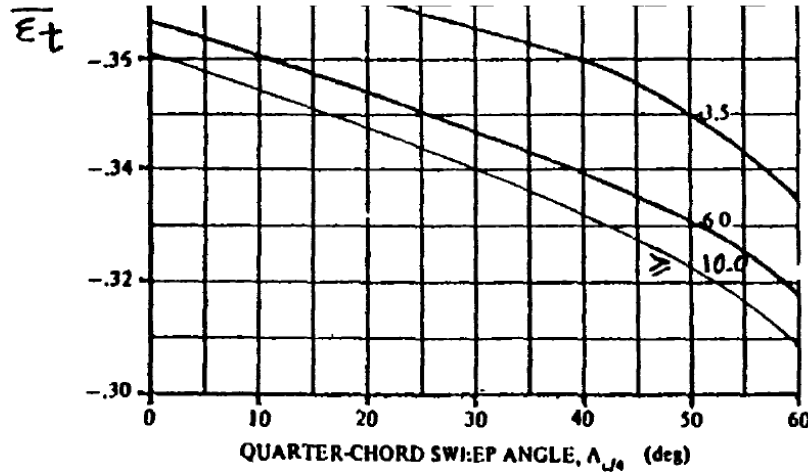


Figure 29: Twist angle based on the $\Lambda_{c/4}$ angle and the AR [2]

19.1.5 Effect of flaps in the wing zero-Lift angle of attack

$$\Delta \alpha_{0L} = \alpha_{0L} \frac{S_{flapped}}{S_{ref}} \quad (54)$$

19.1.6 Parameters affecting the zero Lift angle of attack

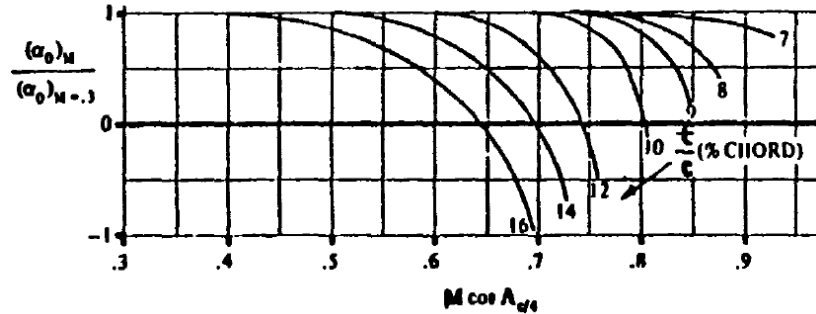


Figure 30: Mach number correction factor of the zero lift angle of attack based on t/c ratio, $\Lambda_{c/4}$ and M [2]

19.1.7 Wing Lift curve slope equation

$$C_{L_{a_{wing}}} = \frac{2\pi AR}{2 + \sqrt{4 + \frac{AR^2\beta^2}{\eta_{airf}^2} \left(1 + \frac{\tan^2(\Lambda_{max})}{\beta^2}\right)}} \frac{S_{exp}}{S_{ref}} F \quad (55)$$

where $\beta = \sqrt{1 - M^2}$ accounts for compressibility effects, $\eta_{airf} = \frac{C_{L_a} M_{airfoil}}{C_{L_a} M_{flatplate}} = \frac{\beta C_{L_a} M_{airfoil}}{2\pi}$, $F = 1.07(1 + d/b)^2$ is the fuselage spillover lift factor.

19.2 Appendix 2

$$\frac{d\epsilon}{d\alpha} = 4.44(K_A K_\lambda K_h \sqrt{\cos(\Lambda_{c/4})})^{1.19} \frac{a_w|_M}{a_w|_{M=0}} \quad (56)$$

$$C_{m_\alpha} f = K_f \frac{L_f W_f^2}{\bar{c} S_w} \quad (57)$$

where:

$$K_A = 1/AR - 1/(1 + AR)^{1.7}$$

$$K_\lambda = (10 - 3\lambda)/7$$

$$K_h = \frac{1 - |h_h/b|}{\sqrt[3]{2l_h/b}}$$

K_f is determine from Figure 31.

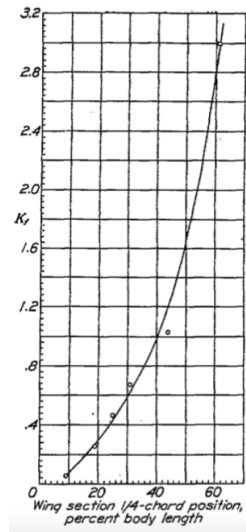


Figure 31: K_f factor determination (experimental data)[4]

19.3 Appendix 3

$$c_{m_0 w} = [c_{m_0 airf}|_{M=0} \left(\frac{AR \cos^2(\Lambda_{c/4})}{AR + 2\cos(\Lambda_{c/4})} \right) - 0.01\epsilon] \frac{a_w|_M}{a_w|M=0} \quad (58)$$

where:

$c_{m_0 airf}$: aerofoil zero-lift pitching moment

ϵ : twist angle in degrees

19.4 Appendix 4

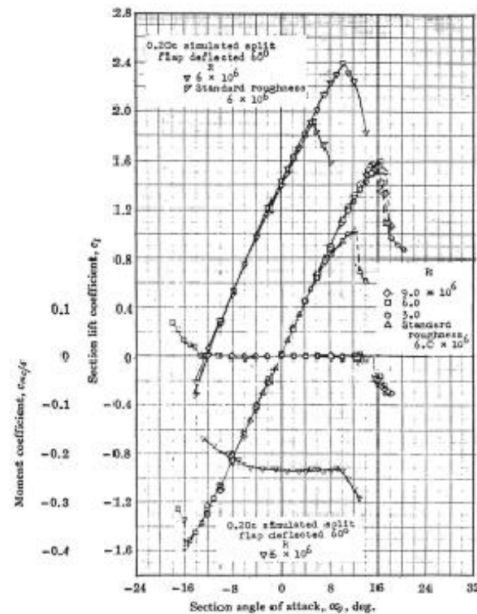


Figure 32: NACA-0012 experimental data [5]

19.5 Appendix 5

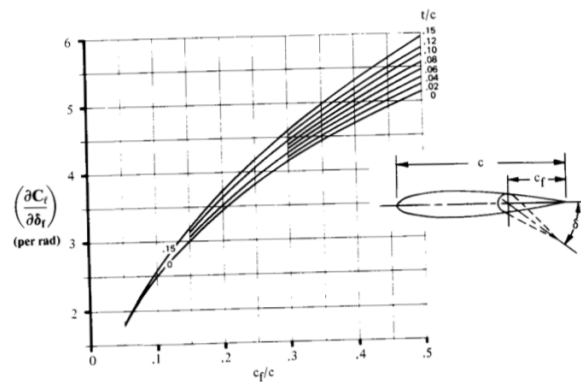


Figure 33: Theoretical lift increment of plain flaps [1]

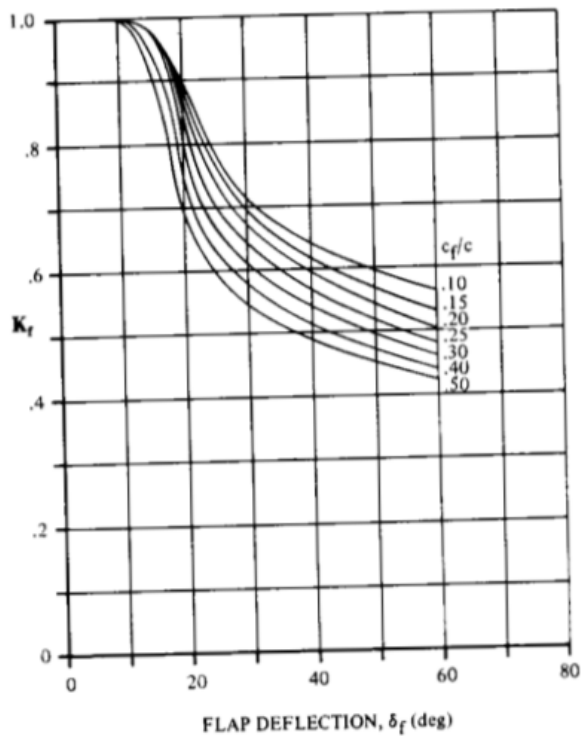


Figure 34: Empirical correction factor[1]

19.6 Appendix 6

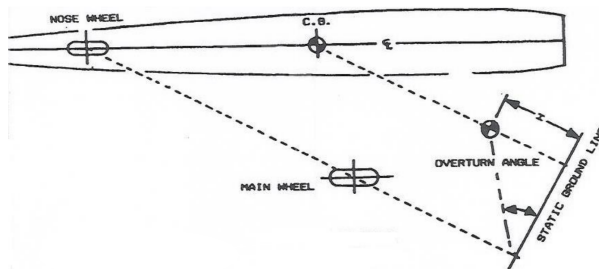


Figure 35: Demonstration of Overturn Angle

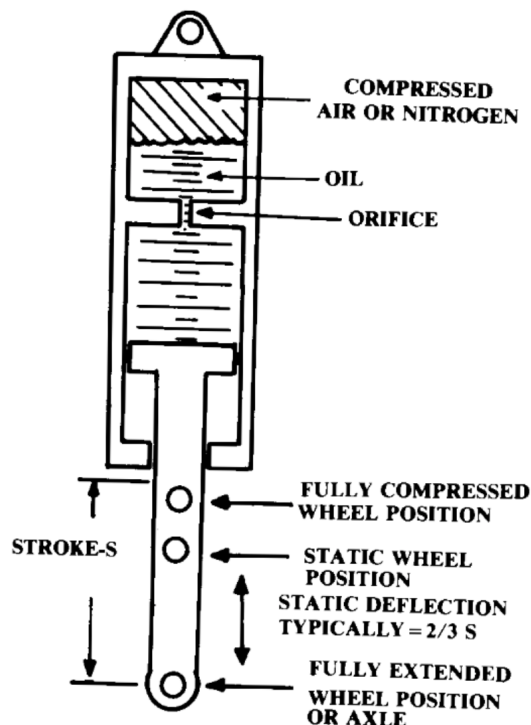


Figure 36: Typical layout of an oleopneumatic shock strut

19.7 Appendix 7

Table 9.1 Typical passenger compartment data

	First class	Economy	High density/ small aircraft
Seat pitch (in.)	38-40	34-36	30-32
Seat width (in.)	20-28	17-22	16-18
Headroom (in.)	> 65	> 65	-
Aisle width (in.)	20-28	18-20	≥ 12
Aisle height (in.)	> 76	> 76	> 60
Passengers per cabin staff (international-domestic)	16-20	31-36	≤ 50
Passengers per lavatory (40" x 40")	10-20	40-60	40-60
Galley volume per passenger (ft ³ /pass)	5-8	1-2	0-1

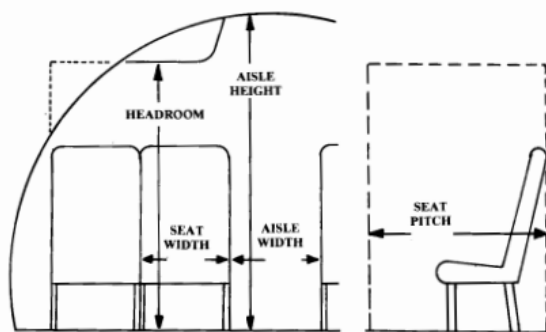
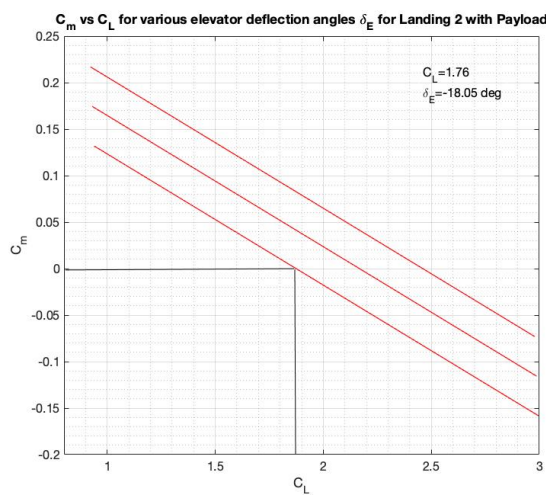


Fig. 9.3 Commercial passenger allowances.



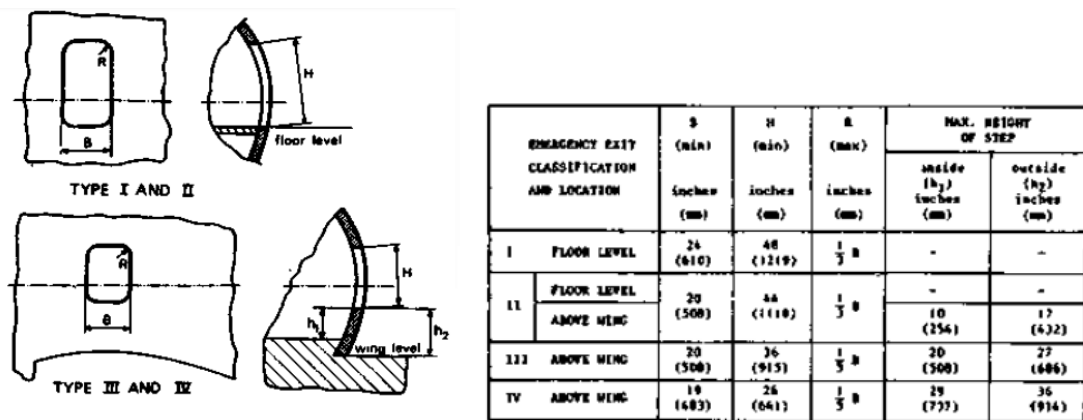
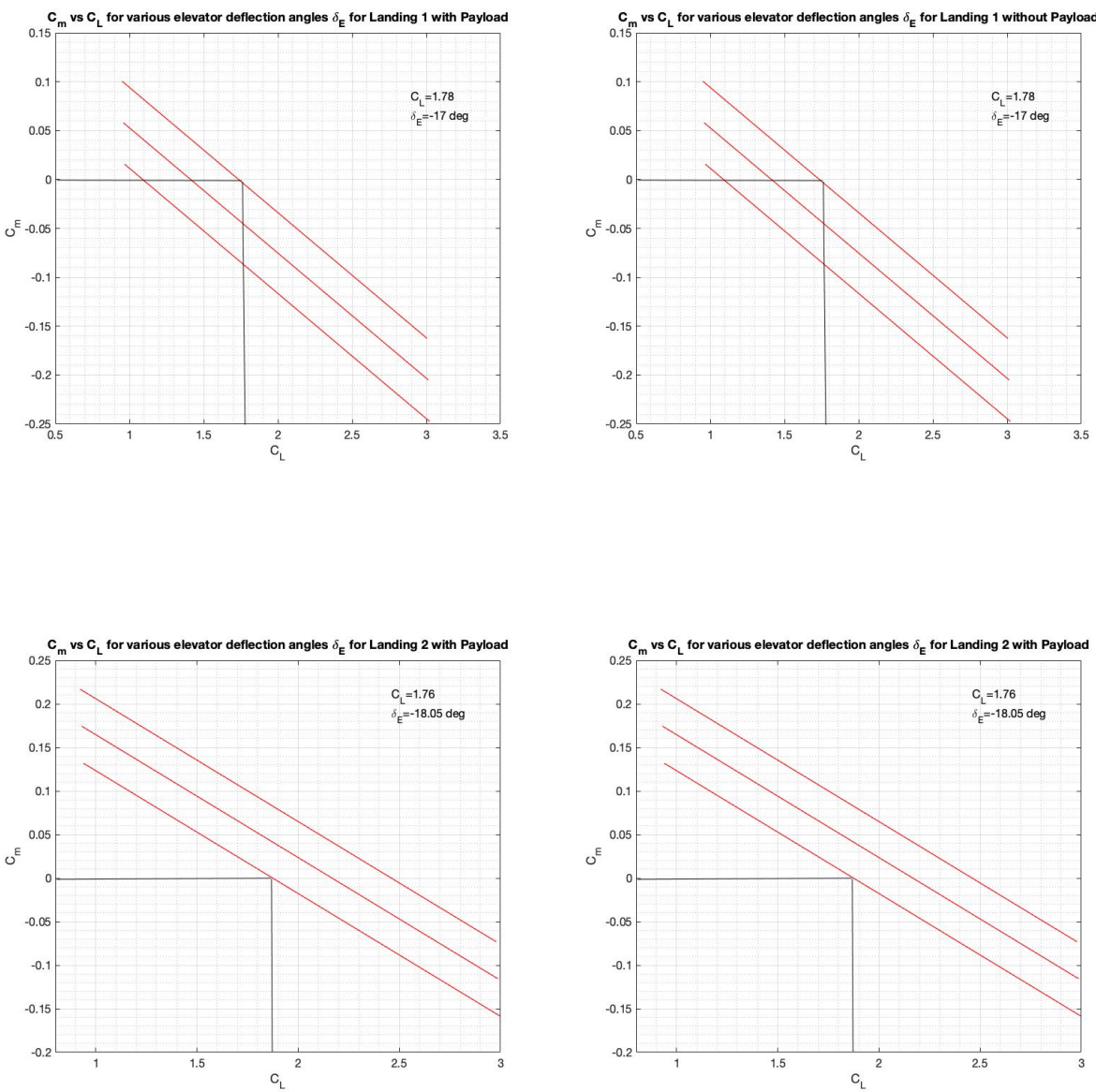
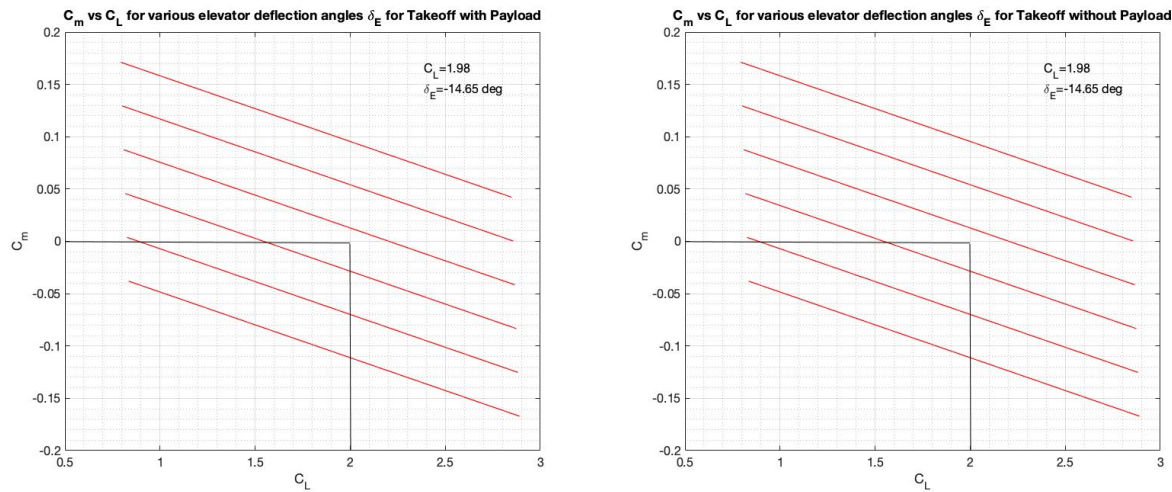


Figure 37: Classification of emergency exits according to [3]

19.8 Appendix 8





19.9 Appendix 9

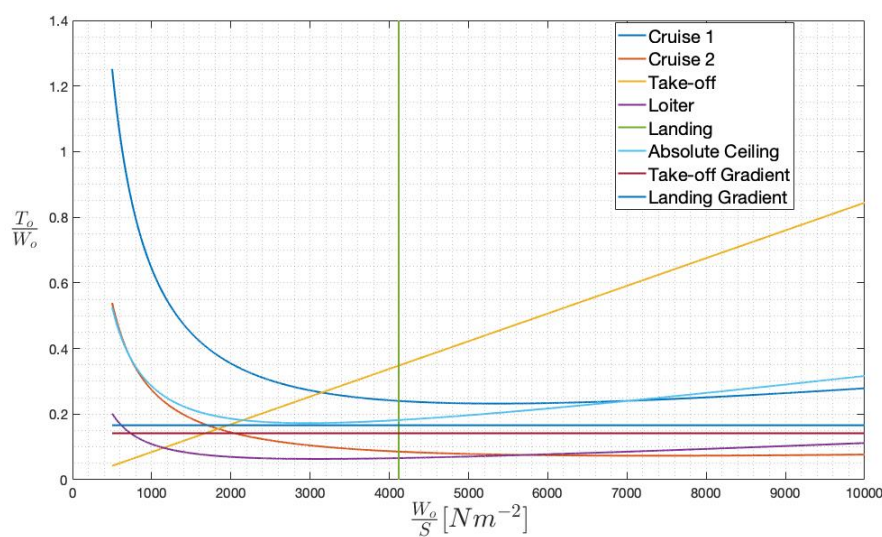


Figure 38: Modified constraint diagram

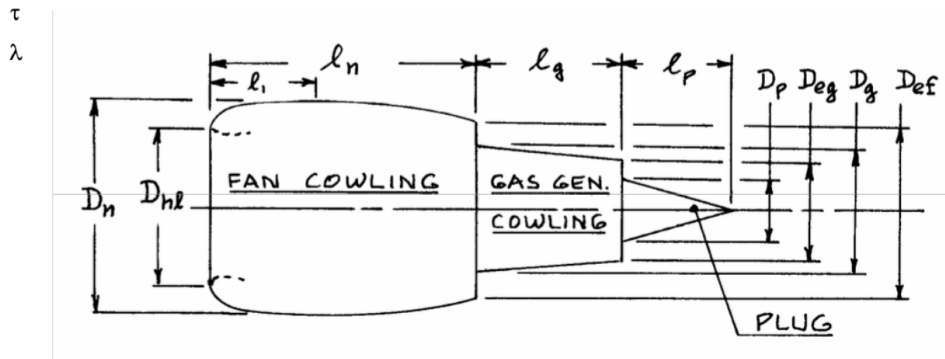
19.10 Appendix 10

$$S_{wet,F} = \pi \cdot d_F \cdot l_F \cdot \left(1 - \frac{2}{\lambda_F}\right)^{2/3} \left(1 + \frac{1}{\lambda_F^2}\right)$$

- d_F Fuselage diameter. For non-circular fuselages D_F is calculated from the fuselage circumference P with $d_F = P / \pi$
 λ_F Fuselage fineness ratio, $\lambda_F = l_F / d_F$.

$$S_{wet,W} = 2 \cdot S_{exp} \cdot \left(1 + 0.25 \cdot (t/c)_r \cdot \frac{1 + \tau \cdot \lambda}{1 + \lambda}\right)$$

- S_{exp} Exposed wing area (without the part of the wing area S_W running through the fuselage).



$$S_{nacelle} = l_n \cdot D_n \cdot \left[2 + 0.35 \frac{l_1}{l_n} + 0.8 \cdot \frac{l_1 \cdot D_{hl}}{l_n \cdot D_n} + 1.15 \cdot \left(1 - \frac{l_1}{l_n}\right) \cdot \frac{D_{ef}}{D_n} \right]$$

19.11 Appendix 11

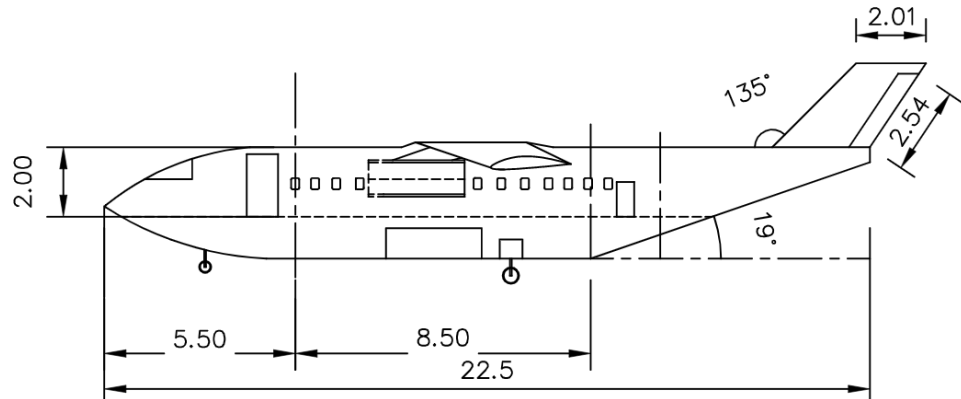


Figure 39: Side View

